An investigation of micro-mechanisms in hydrogen induced cracking in nickel-based superalloy 718

***S.Jothi[1], S. V. Merzlikin[2], T.N.Croft[1], J. Andersson[3,4,5], S. G. R. Brown[1]**
[1]College of Engineering, Swansea University, Bay Campus, Fabian Way, Swansea SA1 8EN, UK
[2]Max-Planck-InstitutfürEisenforschung GmbH, Max-Planck-Straβe 1, 40237 Düsseldorf, Germany
[3]GKN Aerospace Engine Systems, Trollhättan, SE-46181, Sweden
[4]Department of Engineering Science, University West, Trollhättan, SE-46186, Sweden
[5]Department of Materials and Manufacturing Technology, Chalmers University of Technology, Gothenburg, SE-412 96, Sweden
*s.jothi@swansea.ac.uk

ABSTRACT

Superalloys are widely used in a variety of applications including aerospace and land based gas turbine engines and nuclear power plants. The aerospace industry has experienced hydrogen embrittlement problems for many years. Hydrogen embrittlement is a delayed failure mechanism related to loss of ductility due to the presence of hydrogen in the material. Hydrogen embrittlement of the nickel-iron based superalloy 718 has been investigated using slow strain rate tests for pre-charged material and also in-situ hydrogen charging during testing. Fractography analyses have been carried using scanning electron microscopy, electron back-scattering diffraction and orientation image microscopy concentrating on the influence of microstructural features and associated micro-mechanisms leading to hydrogen induced cracking and embrittlement. It was observed that hydrogen induced transgranular cracking initiates at micro-voids in the crystal lattice. Similar behaviour has been observed in multi-scale finite element chemo-mechanical numerical simulations. In contrast, hydrogen induced localized slip intergranular cracking was associated with the formation of micro-voids in intergranular regions. The effects of grain boundary and triple junction character on intergranular hydrogen embrittlement were also investigated. It was observed that low end high angle misorientations (LHAM), $15° < \theta \leq 35°$, and critical high angle misorientations (CHAM), $35° < \theta \leq 50°$, are preferential sites for hydrogen induced cracking. In contrast, few or no hydrogen induced cracks were observed at low angle misorientations (LAM), $0° \leq \theta \leq 15°$, high end high angle misorientations (HHAM), $50° < \theta \leq 55°$, or special GB misorientations (SGB), $\theta > 55°$. Finally, the use of grain boundary engineering techniques to increase the resistance of super alloy 718 to hydrogen induced cracking and embrittlement is discussed.

Keywords: Aerospace Materials; *C*orrosion ; Hydrogen embrittlement; Grain boundaries; Microstructures; Crack mechanics; Electron microscopy; Multiscale modelling and Experimentation;

1. Introduction

Superalloys are widely used in a variety of applications including aerospace and land based gas turbine engines, nuclear power plants and chemical plants. This group of materials possess a range of superior properties in elevated temperature applications which are difficult to obtain from other groups of materials (Francis and Furrer, 2014). Their main advantage is retention of strength at high temperatures (typically $\geq$ 500°C) coupled with adequate ductility. Despite their advantages these alloys are know to be susceptible to degradation caused by the ingress of hydrogen which causes the material to become brittle. The aerospace industry has experienced hydrogen embrittlement problems for many years (Hicks and Alstetter, 1992, Lynch, 2003, Xu et al., 1994). Hydrogen embrittlement is a delayed failure mechanism related to loss of ductility due to the presence of hydrogen in the material. Hydrogen may enter the material during manufacturing processes such as welding or electroplating where this is usually termed 'internal hydrogen embrittlement'. Hydrogen may also enter the material from the surrounding environment during service exposure and this is known as 'environmental hydrogen embrittlement' (Fontana et al., 1986, Martin et al., 2012, Diard et al., 2005, Barbe et al., 2001). Hydrogen is a common fuel in rocket engines and these rocket engines are made of polycrystalline Nickel and Nickel based super alloys 718 especially in combustion chambers. It is well known that hydrogen causes embrittlement in many polycrystalline materials, including high nickel content polycrystalline alloys, and catastrophic failure can occur in hydrogen fuel rocket engine components (Jothi 2015, Reese 2014, Jothi et. al. 2015h, 2015g and 2016).

Alloy 718 is a multi-component alloy containing several alloying elements and is commonly used in the aerospace industry (Preli and Furrer, 2014, Byun and Farrell, 2003, Liu et al., 2002, Mankins and Lamb, 1990). In the aerospace sector Alloy 718 is used in large static casings, as well as in rotating disks used in aero engines, Figure 1. Alloy 718 possesses a complex microstructure which is known to be susceptible to hydrogen embrittlement which can lead to delayed failure.

In terms of microstructure it is known that grain boundaries play a pivotal role in hydrogen induced cracking and embrittlement in polycrystalline metallic materials, including superalloy Alloy718, (Pumphrey, 1976, Randle, 1996, Davies and Randle, 2001, Lejcek et al., 2010, Priester, 2012, Seita et al., 2015, Jothi et al., 2014a, 2014b,

2015b, 2015f). Also, intergranular regions represent preferential sites for crack nucleation and propagation in intergranular hydrogen induced cracking and intergranular hydrogen embrittlement (Kebir and Szummer, 2002, Martin et al., 2012, Jothi et al., 2015a-f, Bechtle et al., 2009). Triple junctions may also play a significant role in the intergranular hydrogen induced cracking in polycrystalline materials. Compatibility stresses at triple junctions may act as preferential sites for cavitation leading to crack nucleation and propagation (Jothi et al., 2015c-d).

Researchers have investigated the metallurgical nature of grain boundaries and intergranular regions in an attempt to correlate microstructural features with an alloy's susceptibility to hydrogen embrittlement and cracking. It has been reported previously that the grain boundary character distribution (GBCD) based on coincidence site lattice (CSL) shows that high angle grain boundaries (HAGBs) act as preferential sites for crack nucleation in polycrystalline materials (Kobayashi et al., 2008, Randle, 1996). Other general reported observations (Lehockey and Palumbo, 1997, Crawford and Was, 1992, Arafin and Szpunar, 2009, Randle, 2004, Seita et al., 2015, Song and Curtin, 2013, Lim et al., 1990) include:

(i) Cracks never nucleate at low angle grain boundary (LAGBs).

(ii) Coherent ($\Sigma 3$) twin boundaries act as potential sites for crack nucleation.

(iii) Twin boundaries provide improved resistance to intergranular cracking in FCC and BCC polycrystalline materials.

The importance of grain boundaries has led to grain boundary engineering methodologies being applied to nickel based super alloys to enhance resistance to fracture (Palumbo and Aust, 1990, Palumbo et al., 1991, Lin et al., 1995, Cheung and Erb, 1994, Kobayashi et al., 2012, Krupp et al., 2003). However, there is still work to be done to fully investigate the connection between intergranular hydrogen induced crack nucleation/propagation and grain boundary and triple junction character. It is also important to investigate the interaction of hydrogen with slip systems in intergranular regions. Despite many studies on hydrogen embrittlement in superalloy Alloy718, very little information is reported on the relationships between the following:

- Micro-mechanisms of hydrogen induced slip localization, intergranular micro-void formation and intergranular hydrogen cracking/embrittlement.

- Micro-mechanisms of micro-void formation in the crystal lattice and hydrogen induced transgranular cracking.
- Grain boundary misorientations, triple junction character and hydrogen induced intergranular cracking phenomena.

In the present study, the main aim is to investigate the points above using slow strain rate tests on hydrogen charged Alloy 718 material coupled to scanning electron microscopy (SEM), electron back-scattering diffraction (EBSD) and orientation image microscopy (OIM) observations of failed material in order to explore ways of increasing resistivity to hydrogen induced cracking/embrittlement.

Ultimately an improved understanding and quantification of these phenomena should give rise to improved computational predictive tools for manufacturing industry, and this is the spirit in which the current work is presented. As will be shown below different types of grain boundaries and combinations of grain boundaries behave quite differently during the ingress and accumulation of hydrogen. Such behaviour needs to be captured correctly both to improve models and also to be able to devise practical methodologies to reduce hydrogen induced failure.

2. Experimental methods:

2.1 Materials and In-situ hydrogen charged tensile test:

A wrought sheet of Alloy 718 was prepared by water jet cutting to produce specimens with gauge length 10.0 mm, width 3.0 mm and thickness 3.2 mm. The specimens were solution heat treated at 954°C for 1 hour and then furnace cooled at a rate of 20°C per minute down to 500°C followed by a normal furnace cooling to room temperature. Slow strain rate testing (SSRT) along the rolling direction (RD) was conducted with two different strain rates of 10^{-4} $s^{-1}$and 10^{-3} s^{-1} at ambient temperature (21°C) using an Instron 8511 hydraulic testing machine. SSRTs were conducted both in air and also using an in-situ hydrogen charging condition. For one benchmark test, no hydrogen charging was carried out and the SSRT was performed in air. For all of the other tests hydrogen was first introduced into the specimens prior to testing with either 4 or 16 hours of pre-charging (i.e. internal hydrogen embrittlement) and then continuous in-situ hydrogen charging was performed during the SSRT (i.e. environmental hydrogen embrittlement) using cathodic charging. Details of the in-situ charging cell for SSRT can be found elsewhere (Koyama et al., 2014). Cathodic

charging was performed in a 3% NaCl aqueous solution containing 3.0 $g.dm^{-3}$ of ammonium thiocyanate (NH_4SCN) at a current density of 10 Am^{-2} using platinum foil as a counter-electrode. Total hydrogen charging time is determined by the addition of the pre-charging time (4 or 16 hours) to the experimental fracture strain divided by the applied strain rate. Hydrogen charging was stopped when the specimen failed. Hydrogen charging during tensile testing introduces external hydrogen efficiently into the samples via hydrogen transport and stress assisted diffusion. After 4 or 16 hours pre-charging it is expected that the internal hydrogen levels will be significant at dislocations, defects, grain boundaries and triple junctions (Martin et al., 2012, Lynch, 2003).

2.2 Material characterization:

The materials were characterised using scanning electron microscopy (SEM) using secondary electron, back scattering electron and electron backscattering diffraction. An Oxford instrument channel 5 HKL system was used for EBSD characterization at a 20 kV accelerating voltage with a probe diameter or beam spot size of 7 nm. A step size of 0.5 µm and 1.0 µm was used in the EBSD analyses. The microstructure observations were conducted one month or longer after the in-situ hydrogen charged tensile tests were carried out. The EBSD data was post-processed using the HKL Tango mapping software.

3. Results and discussions

3.1 Metallographic and EBSD characterization of the undeformed microstructure:

Figure 2 and 3 shows the microstructure of the undeformed solution heat treated Alloy 718. Figures 2 (a) and (b) shows the results of EBSD analysis, crystallographic orientation distribution maps of grain structures as inverse pole figure (IPF) and Euler angle distribution along the rolling direction (RD) of the undeformed material microstructure. Figures 3 (a) and (b) show the Special Coincidence Site Lattice (CSL) grain boundaries (i.e. misorientations $\Sigma<29°$) of the undeformed microstructure and the relative statistics. Table 1 gives the observed percentage values of CSL special grain boundaries (SGBs) for the statistical distribution shown in figure 3 (b). This data shows that 33.3% of grain boundary lengths are $\Sigma3$ SGBs (twin boundaries). 10.32%

of grain boundary lengths are found to be other SGBs. Thus for the solution hardened Alloy 718 a total of 43.62% of grain boundaries are found to be SGBs.

Figure 3 (c) shows the backscattering electron (BSE) SEM image of the undeformed microstructure. The average grain size is 8.17 μm without twin boundaries and the distribution of average grain diameter is shown in figure 3 (c). The average grain size was evaluated from 1447 grains within an area of 179830 μm^2. This study shows that the microstructure of the material prior to testing is free from porosity with relatively homogeneous grain sizes and shapes.

GB Misorientation angle(θ°)	60	36.87	38.94	50.48	61.93	51.68	46.31
CSL /GB Sigma(Σ)	3	5	9	11	17b	25b	29a
Percentage (%)	33.3	0.37	1.9	3.3	0.59	0.42	3.74

Table1: Percentage amounts of Special CSL GBs (Σ<29°) observed in the undeformed solution heat treated superalloy alloy 718.

3.2 Effect of hydrogen on mechanical properties: Results of SSRT tests in air and with in-situ hydrogen charging:

Figure 4 (a) shows the macroscopic engineering stress-strain curves obtained from SSRTs conducted in air and under in-situ hydrogen charging. It can be seen that there is no significant change in yield strength or 0.2% offset yield strength whether samples are tested in air, pre-charged with hydrogen, tested under in-situ hydrogen charging or tested at strain rates of 10^{-3} s^{-1} or 10^{-4} s^{-1}.

From figure 4 (a) it can be seen that the measured UTS values for the hydrogen charged specimens were significantly lower compared to the uncharged specimen tested in air. Ductility was also reduced when decreasing the strain rate from 10^{-3} s^{-1} to 10^{-4} s^{-1} for the hydrogen charged specimens. In terms of strain, the UTS values measured for samples tested with 16 hours hydrogen pre-charging, 4 hours hydrogen pre-charging and without any hydrogen charging (tested in air) occurred at engineering strains of ~37.5%, ~39% and ~45.5% respectively for a strain rate of 10^{-3} s^{-1}. For a strain rate 10^{-4} s^{-1} the UTS of samples tested with 16 hours and 4 hours of hydrogen pre-charging occurred at engineering strains of ~17.5% and ~23% respectively. This indicates that the onset of failure (defined here as the point at which the specimen passes the UTS) begins at lower strains in the hydrogen charged specimens compared to the uncharged specimen. An increase in charging time is expected to increase the uptake of hydrogen while decreasing ductility. Also, the

strain from the UTS to ultimate failure in the uncharged sample tested at strain rate 10^{-3} s^{-1} is ~6% which is greater than the equivalent strain in the hydrogen charged specimen tested at 10^{-3} s^{-1} of ~2%. Figure 4 (b) shows the measured UTS of specimens tested with and without hydrogen charging for the two different strain rates summarising the effects of the various parameters on hydrogen embrittlement.

It can be seen that hydrogen charging time, for the same strain rate, did not significantly alter measured UTS values. However, the specimens charged for 4 hours tested at strain rates of 10^{-3} s^{-1} and 10^{-4} s^{-1} showed a significant drop in UTS for the material tested at the lower strain rate. This is attributed to the increase in testing time for the strain rate of 10^{-4} s^{-1}. This longer time would increase the time for hydrogen trapping at dislocations, raise the local stress and then (i) increases local hydrogen diffusion further and (ii) lead to increased dislocation movement. This deformation also leads to incompatibility stresses along grain boundaries arising from elastic and plastic crystal anisotropy as a function of grain boundary misorientations. This dilatational mismatch between crystals generates further dislocation motion and also increases the mobility and segregation of hydrogen to trap sites (mainly intergranular) as previously reported (Wilcox et al., 1965, Mills et al., 1999). Segregation of hydrogen atoms occurs preferentially at trap sites along highly stressed tensile regions and high stress gradient regions. For longer test durations these hydrogen induced effects are more significant leading to greater embrittlement and lower UTS values for tests extending over longer times, in this case for 10^{-4} s^{-1}.

The strain to failure is also used to assess the hydrogen embrittlement resistance as shown in figure 4 (c). For a strain rate of 10^{-3} s^{-1} the measured failure strains for samples tested with 16 hours hydrogen pre-charging, 4 hours hydrogen pre-charging and without any hydrogen charging were ~39.5%, ~42% and ~52% respectively. For a strain rate of 10^{-4} s^{-1} measured failure strains for samples tested with 16 hours and 4 hours hydrogen pre-charging were~27.5% and ~21.5% respectively. The increase in hydrogen charging time increases the total amount of hydrogen uptake which enhances the dislocation mobility. This reduces ductility leads to a more brittle failure. While these trends are clear it is acknowledged that a greater number of tests would be required to properly quantify experimental scatter. Also, for many industrial applications it is likely that strain rates of 10^{-4} s^{-1} are not particularly slow and again further tests at lower strain rates would be of greater interest.

Figure 4 (d) shows the percentage hydrogen embrittlement ratio (HER) of the hydrogen charged specimens tested at a strain rate of 10^{-3} s^{-1}. The percentage hydrogen embrittlement ratio is a measure of the susceptibility of metallic materials to hydrogen embrittlement. Lower HER values imply lower susceptibility. The HER value (units: %) is calculated using below shown equation (1).

$$HER = \left(\frac{\varepsilon_{air} - \varepsilon_{hydrogen}}{\varepsilon_{air}} \right) \times 100 \quad (1)$$

Here ε_{air} is the failure strain for a specimen tested in air and $\varepsilon_{hydrogen}$ is the failure strain of a specimen tested under hydrogen charging conditions. The results in figure 4 (d) show the effect of hydrogen in reducing the ductility of solution heat treated superalloy Alloy 718 with the longer charging time resulting in a higher HER. In summary, the sample without hydrogen is most ductile and samples charged with hydrogen display lower failure strains.

3.3 SEM Fractography of Alloy 718 failed specimens:

Figure 5 (a) shows the secondary electron (SE) image obtained from SEM of the fractured samples of the uncharged SSRT test conducted in air. One primary crack has led to failure and no secondary cracks were observed. Figures 5 (b) and (c) show the fractured specimens from SSRT tests with 16 hours hydrogen pre-charging for strain rates of 10^{-3} and 10^{-4} s^{-1} respectively. In stark contrast to the uncharged specimen there are many secondary surface and subsurface cracks visible in the hydrogen charged specimens. The observed secondary cracks are largely perpendicular to the loading direction. Local grain boundary cracking has been reported to arise perpendicular or at 45° to the loading direction (Masayuki et al., 2007, Pouillier et al., 2012). Larger secondary cracks are observed on the surface of samples tested at strain rate 10^{-4} s^{-1}compared to samples tested at strain rate 10^{-3} s^{-1}. A decrease in strain rate increases the time duration of the test, which will increase the amount and depth of hydrogen diffusion into the sample specimen and this corresponds to the amount of subsurface cracks observed.

For the uncharged specimen figures 6 (a) and (b) show the macro-scale cross section of the fracture sample and micro-scale fracture surface of the sample respectively. Figure 6 (b) shows a typical ductile fracture surface. Figures 6 (c) and (d) show the fracture surfaces of the specimens tested with 16 hours hydrogen pre-charging at the macro and micro scales respectively. The fracture surface shows outer

regions of brittle fracture and inner regions of ductile fracture. Brittle fracture surfaces were observed near the edge of the specimen to a depth of ~1 mm while ductile fracture surfaces were observed towards the centre of the specimen. Considering the diffusivity of hydrogen in the alloy, there is not enough time for hydrogen to fully diffuse to the centre of the specimen. Thus central regions of the specimen are more likely to fracture in a ductile mode. The hydrogen induced brittle modes of fracture appear to be intergranular supporting the idea that grain boundaries and triple junctions are more susceptible to hydrogen induced cracking compared to the grain interior lattice.

Figures 7 (a), (b) and (c) are a series of fracture surface images at increasing magnification. Figure 7 (a) shows both transgranular and intergranular cracking. Most of the crack paths observed are intergranular with only very few transgranular cracks. Figures 7 (b) and (c) show the hydrogen induced transgranular crack propagation path. From a previous multi-scale FE stress assisted hydrogen diffusion numerical model (Jothi et al., 2015c,d and f) it was observed that the presence of voids or pores in the grain lattice leads to high stress concentrations which act as a driving force for the segregation of hydrogen near the edges of these voids, perpendicular to the traction direction. This leads to crack initiation at the edges of the void and these cracks propagate in a transgranular manner. Such pores in the lattice may arise from manufacturing processes or could possibly develop from the accumulation of dislocations, hydrogen and vacancies within the lattice associated with applied stress.

The numerical model mentioned above is a microstructural coupled multi-scale FE model and multi-scale FE chemo-mechanical analysis of void/pores microstructures (Jothi et al., 2015 c, f) . The model incorporates microscale stress-assisted diffusion of hydrogen with different diffusivities and grain boundary energies for different regions of microstructure (grain interiors, different types of grain boundary regions, triple junctions). The relative proportions of these regions are also adjustable in the model which has been shown to correctly match diffusion experiments. In order to investigate the effect of voids on hydrogen induced failure mechanisms, multi-scale FE chemo-mechanical stress-assisted hydrogen diffusion simulations were carried out on representative microstructural volume elements (RMVE). The RMVE model was developed in ABAQUS FE software by incorporating the real microstructural master database developed using MATLAB and PYTHON coding from the following datasets i.e crystal orientation dataset, grain

boundary characteristic distribution dataset, misorientations dataset, grain size distribution dataset and grain structure extracted from experimental EBSD analysis results. The master database developed by processing the machine logged data source using ETL (Extraction-transformation-loading) including cleansing, reformatting, and integration and finally inserted into data warehouse. This data warehouse will be used to incorporate the structured multiscale computational modelling data sources, manufacturing process data and also other experimentally collected machine data sources from atom probe analysis, detect material testing and material characterization, electrochemistry analysis and mechanical testing etc.. This data warehouse then will be incorporate with unstructured data including streaming manufacturing process real-time sensor data in order to study and investigate the structure-property-manufacturing process-application analysis of materials including failure analysis and also to develop materials and new alloys based on data science data driven approach. One such example; In EU FP7 "MultiHy" project lots of big data sets were collected on AIRBUS Ariane 5 space rocket composition chamber materials from various sources from streaming manufacturing machine senor data sources such as electroplating, welding, machine logged data source from material and microstructural characterizations such as EBSD analysis, SEM images, electrochemical and mechanical testing machine data source, and multi-scale modelling data sources to predict the failure analysis due to hydrogen embrittlement and more details about it can be found elsewhere (Jothi et. al. 2016, Jothi 2015, Jothi et. al. 2015h). Figure 8 (a) and (b) shows the microstructural image developed from the experimental EBSD analysis machine logged data sources. Figure 8 (a) shows the grain distribution, morphology and crystal orientation. Figure 8 (b) shows the grain boundary characteristics distribution and figure 8 (c) shows the colour code of the GBCD. Detailed information on the development of ABAQUS real microstructural representative multi-scale FE model by incorporating the EBSD machine data source including algorithm and procedure are described elsewhere (Jothi et al., 2015f, 2015d).

ABAQUS multiscale FE model were developed from the EBSD machine data source using MATLAB, PYTHON coding then meshed with fine elements using FE code and subsequently, voids were randomly introduced into the grain boundaries on this mesh as shown in the figures 8 (d). Multiscale chemo-mechanical simulations for bi-crystal and polycrystalline nickel microstructures served as a motivation for this

study (Jothi et al., 2015d, a, c and 2014a). The simulation procedure consists of an initial elastic-plastic stress analysis and then calculated stresses are used in a stress-dislocation assisted hydrogen diffusion analysis. A brief description of this procedure is given here. Detailed information about the numerical implementation of the above constitutive approach for multiscale FE can be found elsewhere (Jothi et al., 2015d, a, c and 2014a). In the finite element stress-assisted hydrogen diffusion analysis, the hydrogen flux vector (J^{α}) consists of flux generated by the hydrogen concentration gradient (J_c^{α}) and the hydrostatic stress gradient (J_h^{α}) as shown below:

$$J^{\alpha} = J_c^{\alpha} + J_h^{\alpha} = -D\nabla C + \frac{DV_h}{RT} C\nabla\sigma_h \tag{2}$$

$$\therefore \frac{\partial C}{\partial t} = -divJ^{\alpha} = sD\Delta\phi - \frac{DV_h}{R(T-T_0)} s\phi\Delta\sigma_h - \frac{DV_h}{R(T-T_0)} s\nabla\phi\nabla\sigma_h \tag{3}$$

Where R is the gas constant, *(T-T0)* is absolute temperature, $\Delta\phi = \sum_{\alpha} \frac{\partial^2\phi}{\partial x_{\alpha}^2}$, Δ is the Laplace operator, α = G, GB, TJ, DI, representing different localized regions in the microstructure (G is crystal lattice sites, GB is grain boundary sites, TJ is triple junctions, DI is dislocations). The diffusivity of hydrogen depends on the activation energy as shown below:

$$D = \left[\gamma . a_0^2 v \exp\left(\frac{\beta\Delta H}{RT_{mp}}\right)\right] . exp\left(\frac{-E_a}{R(T-T_0)}\right) \tag{4}$$

Where E_a is the activation energy and the pre-factor is

$$D_0 = \gamma . a_0^2 v \exp\left(\frac{\beta\Delta H}{RT_{mp}}\right) \tag{5}$$

Here γ is the geometric factor, a_0 is the jump distance, v is the frequency with which the solute atom vibrates in the diffusion direction, ΔH is the activation energy for diffusion, T_{mp} is the melting point of the pure metal, $\beta = \frac{d\left(\mu/\mu_0\right)}{d\left(T/T_{mp}\right)}$, μ is the elastic modulus of the pure metal and μ_0 is the elastic modulus at zero degrees absolute (Harris, 1989, Jothi, 2015). The effective diffusion of hydrogen in the bulk material can be calculated using a finite element microstructure homogenization method and meso-scale microstructure computational simulation of hydrogen permeation tests (Jothi et al., 2014b, 2015f). Other terms are *s*, the solubility of hydrogen, V_h is the partial molar volume of hydrogen, C is the hydrogen concentration and σ_h is the hydrostatic stress given by

$$\sigma_h = \frac{1}{3}\left(\sigma_x + \sigma_y + \sigma_z\right) \tag{6}$$

C/s is the normalized hydrogen concentration which is dependent on the hydrostatic stresses as given in the equation below.

$$\phi = \phi_0 exp\left(\frac{-V_h \sigma_h}{R(T-T_0)}\right) \quad (7)$$

Where the unstressed state of the normalized concentration under the condition of hydrogen-metal equilibrium is ϕ_0.

Then the trap model is incorporated in the stress assisted hydrogen diffusion analysis and the details explanation about the trap model can be found elsewhere (Jothi et. al., 2015g). A simulation result using this model is shown in figures 8 (e) and (f). Figure 8 (e) shows the calculated stress field in a representative 2D micro-scale region containing pre-existing voids in the microstructure. In this figure tensile stresses at void surfaces perpendicular to the loading direction are formed. Figure 8 (f) shows the predicted hydrogen segregation occurring preferentially in these same regions of tensile stress. Regions under high tensile stress possessing higher hydrogen concentrations would represent likely crack initiation sites. Tensile stresses developing around voids/pores could act as a mechanism to drive pore growth through the crystal lattice forming transgranular cracks and promoting the type of failure shown in figures 7 (a), (b) and (c). Furthermore, a recent thermo-mechanically coupled-theory predicted a higher lattice hydrogen concentration at crack-tips due to the effect of the tensile volumetric strains at the same location (Di Leo and Anand, 2013).

3.4 Effect of grain boundary misorientation types on hydrogen segregation at grain boundaries in IN718 polycrystalline material:

Figure 9 (a), (b) and (c) shows the EBSD result image of IN718 microstructure, grain boundary characteristics distribution based on misorientation types and real microstructural based representative volume element FE model respectively. Chemo-mechanical-dislocation-microstructural multiscale FE model developed using real microstructure RVE in the absence of pores were employed to investigate the hydrogen induced crack initiation leads to the hydrogen embrittlement failure analysis. Results of stress-dislocation-microstructural assisted hydrogen diffusion analysis are shown in figure 9 (d). This preliminary result shows large accumulations of hydrogen along CHAM and LHAM type grain boundaries with less

accumulation along LAM, HHAM and SGB type grain boundaries. The higher hydrostatic stresses developed between neighbouring grains with CHAM and HHAM type grain boundaries give rise to higher amounts of hydrogen trapped in these regions compared to neighbouring grains with LAM, HHAM and SGB type grain boundaries. Greater accumulation of hydrogen at CHAM and LHAM boundaries would make these regions more susceptible to crack initiation and propagation because they would exceed any given critical hydrogen concentration much earlier than LAM, HHAM and SGB type grain boundaries. The elastic single crystal properties of superalloy used to each grains are C_{11}=231.2, C_{12}=145.1 and C_{44}=117.2 (GPa) and the plastic properties are extracted from the stress strain curve shown in figure 3(a). The single crystal superalloy elastic values are close to single crystal pure nickel anisotropic values (Haldipur et al., 2004, Jothi et al., 2014a, 2015c, 2015d, Haldipur, 2006, Leidermark, 2011). The properties of hydrogen diffusion in nickel and IN718 can be found elsewhere. (Xu et al., 1994, Jothi et al., 2015d,f, Jebaraj et al., 2014).

Figures 10 (a) and (b) show an intergranular crack propagation path (with slip traces, some highlighted with white dotted lines) and the presence of carbides in the crack path. The two black arrows in figure 10 (a) show two different slip systems acting across a grain boundary very similar to previous observations in pure nickel (Martin et al., 2012). Figure 10 (b) shows a magnified view of slip traces on a fracture surface on an intergranular crack propagation path. The majority of the crack propagates along the intergranular region where hydrogen trapping will be greater indicating that the intergranular region and voids are preferential sites for hydrogen trapping compared to lattice sites. Intergranular sites provide routes of higher hydrogen mobility as they are a lower energy barrier to hydrogen diffusion and would possess lower activation energy of hydrogen desorption compared to hydrogen lattice sites. Such segregation and trapping of hydrogen along grain boundaries has previously been observed using secondary ion mass spectroscopy for hydrogen diffusion in pure nickel (Fukushma and Birnbaum, 1984, Ladna and Birnbaum, 1987). The slip traces on both sides of two crystals intersecting across grain boundary indicates the presence of dislocations that can also act as trapping sites for hydrogen. This causes intergranular plasticity leading to intergranular brittle cracking often referred to as the hydrogen enhanced localized plasticity (HELP) mechanism of hydrogen embrittlement. All these observations indicate that plastic processes due to

slip localization are an important micro-mechanism of hydrogen induced intergranular embrittlement in Alloy 718. Figure 10 (b) also shows the segregation of carbon in the intergranular region.

Segregation of carbon atoms at grain boundaries in alloy 718 were observed in atomic scale investigations using atom probe tomography (APT) as shown in figure 11 (a) (Jothi, 2015e). It has been previously reported that carbon at grain boundaries/micro-cracks can combine with hydrogen to form methane and this has been included in numerical models (e.g. Schlögl and Giessen, 2001). This enhances micro-crack initiation along grain boundaries. Void formation along intergranular interfaces can be seen in figure 11 (b). It has also been previously reported that segregation of impurity atoms also induces intergranular hydrogen embrittlement in a nickel based superalloy (Byun and Farrell, 2003, Ladna and Birnbaum, 1987).

Figure 11 (c) shows hydrogen assisted crack initiation and a slip band system consistent with intergranular strain localization and the HELP mechanism. The slip bands in the intergranular region were enhanced by hydrogen uptakes due to high stress concentrations. Intergranular slip takes place at grain boundaries and also by gliding on slip planes just below the boundaries, Clusters of hydrogen atoms can form in these regions particularly at vacancies. Increasing the density of vacancies promotes the formation of micro-voids along the intergranular region. The formation of micro-voids increases the internal gas pressure within voids due to the formation of molecular hydrogen. High hydrostatic tensile stresses around voids acts as a driving force to increase the diffusion of hydrogen towards the void with a higher concentration of hydrogen atoms becoming trapped near the micro-void edges perpendicular to the loading direction. These pressure stresses depend on the size/area of the micro-voids. In this respect Schlögl and Giessen present a multi-scale micromechanics modelling for chemico-mechanical damage processes at sub-micron scales coupled to macroscopic behaviour via a series of size-scale transitions (Schlögl and Giessen, 2001). However, the common assumption in numerical models that grain boundaries are all identical could be improved upon given the results described below. The intergranular trapped hydrogen softens the intergranular region by decreasing the cohesive energy between lattice atoms near the grain boundary. This leads to micro-void expansion and merging together and coarsening of neighbouring micro-voids. Recent work has shown that the formation of a gas pressure inside a void leads to a bubble growth process and hydrogen induced failure (Fischer and Svoboda, 2014).

Growth of micro-voids on the slip lines in the intergranular region may initiate cracks at triple junctions and/or larger micro-void sites, propagating along intergranular regions. This mechanism is illustrated schematically in figures 11 (d) to (i).

While intergranular failure modes are predominant in this work there are also a few transgranular failures observed. To attempt to explain the transgranular failure mode and based on the experimental results we propose a mechanism for hydrogen induced transgranular cracking based on micro-void crack growth shown schematically in figure 12. The edges of deformed micro-voids perpendicular to the loading direction in the crystal lattice act as preferential sites for transgranular crack initiation. Initially a Stage 1 crack propagates by the formation and coalescence of voids. At a certain crack length Stage 2 propagation occurs driven towards intergranular regions where the lattice will be more disordered and there will be higher concentrations of hydrogen.

3.5 Micro-scale investigation of hydrogen induced crack nucleation and crack propagation paths using SEM-EBSD analysis:

The main aim of this EBSD investigation is to understand relationships between grain boundary (GB) misorientation and hydrogen induced intergranular crack nucleation and propagation in Alloy 718. In this study, hydrogen induced cracking is related to grain boundary character distribution (GBCD) as defined by grain boundary misorientation angles (irrespective of axis plane). Five different types are defined according to GB misorientation angle below.

(1) Low angle GB misorientations (LAM) ($0° \leq \theta \leq 15°$)

(2) Low end High angle GB misorientation (LHAM) ($15° < \theta \leq 35°$)

(3) Critical High angle GB misorientation (CHAM) ($35° < \theta \leq 50°$)

(4) High end High angle GB misorientation (HHAM) ($50° < \theta \leq 55°$)

(5) Special GB misorientation (SGB) ($55° < \theta$)

The uncharged and hydrogen charged fractured specimen microstructures on the wider face of the gauge length section, parallel to the loading direction, were examined as shown in figures 13, 14, 15 and 16. EBSD scans were performed in the vicinity of the micro-crack front over areas of $490 \times 367\ \mu m^2$ and $153 \times 114\ \mu m^2$ on uncharged and charged specimens respectively. Figures 13 (a) and (b) show the uncharged fractured specimen indicating that preferential crack propagation was

transgranular and no sub-cracks were observed. A crystallographic orientation map and IPF is shown in figure 13 (a). Figure 13 (b) shows the local misorientation map (with red regions having high levels of local misorientation and blue regions having lower amounts). Local misorientations are higher along the fracture path due to the higher local deformation and fracture is mostly transgranular.

Figure 14 (a) shows hydrogen charged SSRT tested fractured specimen, figure 14 (b) shows the EBSD map overlaid on the SEM micrograph and figure 14 (c) shows the corresponding local misorientation map. Figure 14 (b) shows that preferential crack propagation for hydrogen charged SSRT tested specimen was intergranular with many macroscopic sub-cracks observed perpendicular to the loading direction with a few micro cracks observed parallel to the loading direction. High local misorientations are observed in the intergranular cracked region. Considering figures 14 (a-c) it is clear that grain boundaries and triple junctions have been deformed more than the internal crystal lattice. Figure 15 (a) shows the crystallographic orientation and IPF image. Intergranular cracks are mostly perpendicular to the loading direction. Figure 15 (b) shows a magnified view of a region near a sub-crack with Euler angles. Figures 16 (a, b and c) can be used to attempt to understand the effect of grain boundary character distribution on intergranular hydrogen embrittlement. These results show that the cracks are intergranular with CHAM-type regions observed along the crack path. Also, some likely crack nucleation points can be identified at triple junctions displaying CHAM-CHAM-SGB and CHAM-CHAM-CHAM connectivities. It has previously been observed in experimental studies and numerical models that certain types of triple junction are more susceptible to hydrogen embrittlement and therefore more likely to provide crack nucleation points (Koyama et al., 2013, Jothi et al., 2015c, Chen et al., 2000, Meyers and Chawlu, 2009).

An attempt was made to quantify the effect of grain boundary misorientation character and triple junction character on hydrogen induced intergranular cracking. Hydrogen induced intergranular cracks were observed at 103 grain boundaries. 58.3% of the grain boundaries within cracks were CHAM, 35% were LHAM, 4.9% were HHAM and 1.9% were SGB. This data is summarised in figure 17. Interestingly, no intergranular cracks were associated with LAM. Thus LAM, HHAM and SGB are the types of GB misorientations where few or no hydrogen induced cracks were observed. This is attributed to the lower stress concentrations and lower hydrogen trapping characteristics of these types compared to LHAM and CHAM. These results are also

consistent with previous numerical model findings for a bi-crystal pure nickel investigation (Jothi et al., 2014a).

During testing localized stress concentrations in the microstructure will arise due to crystal anisotropy. Tensile stresses are accumulated on CHAM and LHAM regions which act as a driving force for hydrogen atoms to form in more concentrated clusters preferentially along CHAM and LHAM regions compared to other sites. Hydrogen trapping in CHAM and LHAM regions reduces the ductility along these grain boundaries due to a reduction in cohesive energy. Once the trapped hydrogen in the CHAM and LHAM exceeds a critical value it results in intergranular hydrogen embrittlement. This behaviour was previously reported in electrodeposited annealed nickel with a combination of multi-scale microstructural modelling and experimental observation (Jothi et al., 2015d). In total 93.3% of hydrogen induced intergranular cracks were observed in CHAM/LHAM boundaries indicating that these types of boundary are the most susceptible sites for hydrogen induced cracking in Alloy 718. Hydrogen enhances plastic flow by increasing the dislocation mobility. Dislocation mobility will be higher along the intergranular regions due to the increased amount of hydrogen segregation, which will increase the plastic flow but at the same time reduce the local ductility when compared to the crystal lattice. This will also depend on the grain boundary types. For example, in low angle grain boundaries plastic flow is relatively slower due to lower dislocation mobility arising from lower amounts of hydrogen segregation in these regions compared to higher angle grain boundaries where dislocation mobility (and hydrogen segregation) will be higher. These results also suggest that LAM, HHAM and SGB grain boundary misorientations are effectively more resistant to intergranular hydrogen embrittlement (IHE) with the LAM GB misorientation having the greatest resistance in Alloy 718. Based on this observation, GB types are now categorised into two types, resistant (R-type) and susceptible (S-type), as given below.

- R-type: IHE-resistant grain boundaries = LAM, HHAM, SGB
- S-type: IHE-susceptible grain boundaries = LHAM, CHAM

With this definition triple junction connectivity (TJC) can be classified into four different types depending on the possible combinations of R- and S-types at the junction.

1. TJ0 type TJC with zero R-type connectivity = S-S-S

2. TJ1 type TJC with one R-type connectivity = S-S-R
3. TJ2 type TJC with two R-type connectivity = S-R-R
4. TJ3 type TJC with three R-type connectivity = R-R-R

It has been previously reported that triple junctions play a significant role in hydrogen diffusion and hydrogen induced cracking (Jothi et al., 2015c, 2015d, Chen et al., 2000) and so now we can consider the effect of TJC on hydrogen induced cracking in Alloy 718. Figure 18 shows the relationship between hydrogen induced cracking (HIC) and TJC. The HIC data were taken from 62 different triple junctions. 51.6% of hydrogen induced TJ cracks were detected at TJ0-type triple junctions. 40.3% and 8.1% of TJ cracks were observed at TJ1-type and TJ2-type TJCs respectively. No cracks were observed at TJ3-type triple junctions. This indicates that TJs containing the more susceptible GBC connectivities, such as TJ0-type and TJ1-type, are more likely sites for hydrogen induced cracking. TJ3-type triple junctions appear to be much more resistant to hydrogen induced cracking. Thus hydrogen induced cracking at triple junctions strongly depends on nature of the triple junction connectivity.

3.6 Control of hydrogen induced cracking/ embrittlement by grain boundary engineering (GBE):

Transgranular hydrogen induced cracking can be controlled by reducing the formation of micro-voids/pores in the crystal lattice during manufacturing. One way of controlling intergranular hydrogen embrittlement is by reducing the segregation of carbon atoms along the intergranular region. This can be achieved by adding small amounts of elements such as titanium, niobium and vanadium. Reducing the segregation of carbon atoms along the intergranular region should enhance the ductility and reduce the susceptibility of intergranular hydrogen induced cracking in Alloy 718.

Another possibility is grain boundary engineering. Watanabe introduced the concept of grain boundary engineering and design three decades ago to improve the ductility of materials (Watanabe, 1984). Grain boundary engineering often involves low temperature heat treatment to induce limited grain growth and rearrangement of grain boundaries. Palumbo et al. have used grain boundary engineering to improve intergranular stress corrosion cracking resistance (Palumbo and Aust , 1990, Palumbo et al., 1991, Lin et al., 1995, Lehockey et al., 1999). Qian and Lippold used a GBE approach to control heat affected zone liquation cracking in superalloys, including

Alloy 718, (Qian and Lippold, 2003) and other workers have used grain boundary engineering design and control to improve material performance (Thaveeprungsriporn et al., 2001, Watanabe, 1993, Palumbo and Aust, 1995, Fionova et al., 1996, Davis et al., 2001, Randle and Davies, 2002, Alexandreau et al., 2001, Lee and Richards, 2003). Collins and Stone describe a computational predictive tool capability which was used to optimise the post-forging heat treatment of forged RR1000 nickel-base superalloy and improve proof stress (Collins and Stone, 2014).

The authors are unaware of such treatments being applied specifically to improve hydrogen embrittlement susceptibility in alloys. From this paper it seems clear which grain boundary misorientations and triple junction types are more or less susceptible to hydrogen induced problems. It is suggested that grain boundary engineering approaches would be an interesting area for future study for alloy 718 in particular to assess the feasibility of increasing the fraction of LAM, HHAM and SGB GBs in Alloy 718 using grain boundary engineering techniques in order to increase its resistivity to hydrogen embrittlement. The preliminary results in this work would suggest that a more detailed SSRT data set combined with a systematic investigation of grain boundary engineering treatments could be of significant benefit in this field. One problem in this endeavour would be to quantify the hydrogen distribution within a material. Unfortunately atom probe tomography is not able to provide such data. The use of scanning Kelvin probe force microscopy techniques offers some promise and this is work currently in progress. One might also suggest the use of deuterium; however the diffusivity of deuterium may well be different from the common hydrogen isotope, protium.

4. Conclusion

Hydrogen induced intergranular, transgranular cracking and hydrogen induced localized intergranular plasticity and the effect of grain boundary character (GBC) and triple junction connectivity (TJC) in polycrystalline superalloy 718 were investigated using in-situ hydrogen charged slow strain rate tests. It was found that hydrogen induced cracking strongly depends on the nature of GBCs and TJCs. The results indicate for alloy 718:

(a) The ultimate tensile strength and tensile ductility are significantly reduced by in-situ hydrogen charging during tensile testing.

(b) Nucleation and growth of micro-voids/pores in the crystal lattice are initiation sites for hydrogen induced transgranular cracking.

(c) Slip localization from micro-voids in intergranular regions leads to hydrogen induced intergranular cracking.

(d) Hydrogen induced cracking was mostly associated with grain boundaries having misorientations in the range $15° < \theta \leq 50°$. No cracks were observed at low angle ($0° \leq \theta \leq 15°$) grain boundary misorientations.

(e) Hydrogen induced intergranular cracks were observed predominantly at TJ0-type and TJ1-type triple junctions and not observed at all at TJ3-type triple junctions.

Acknowledgements

This work was supported by EU 7th framework program through the project MultiHy (Multiscale Modelling of Hydrogen Embrittlement) under project no. 263335. The author S. Jothi also gratefully acknowledges the assistance of the MACH1 Laboratories in-terms of SEM sample preparation at Swansea University.

References:

Alexandreanu, B., Capell, B., Was, G.S., 2001, Combined effect of special grain boundaries and grain boundary carbides on IGSCC of Ni-16Cr-9Fe-xC alloys, Materials Science and Engineering A 300, 94.

Arafin, M.A., Szpunar, J.A., 2009, A new understanding of intergranular stress corrosion cracking resistance of pipeline steel through grain boundary character and crystallographic texture studies, Corrosion Science, 51, 119.

Barbe, F., Forest, S., Cailetaud, G., 2001, Intergrangular and intragranular behavior of polycrystalline aggregates. Part 2. Results, International Journal of Plasticity, 17, 537.

Bechtle, S., Kumar, M., Somerday, B.P., Launey, M.E., Ritchie. R.O., 2009, Grain-boundary engineering markedly reduces susceptibility to intergranular hydrogen embrittlement in metallic materials, Acta Mater., 57, 4148.

Byun, T.S, Farrell, K, 2003, Tensile properties of Inconel 718 after low temperature neutron irradiation, Journal of Nuclear Materials, 318, 292.

Chen, C.R., Li, S.X., Wen, J.L., Jia, W.P., 2000, Finite element analysis about effects of stiffness distribution on stresses and elastic strain energy near the triple junction in a tricrystal, Materials Science and Engineering A 282, 170.

Cheung, C., Erb, U., 1994, Application of grain boundary engineering concept to alleviate intergranular cracking in Alloys 600 and 690, Materials Science and Engineering A 185, 39.

Collins D.M., Stone H.J., 2014, A modelling approach to yield strength optimisation in a nickel-base superalloy, Int. J. Plasticity, 54, 96.

Crawford. D.C., Was. G.S., 1992, The role of grain boundary misorientation in intergranular cracking of Ni-16Cr-9Fe in 360°C argon and high purity water, Metall. Mater. Trans. A 23, 1195.

Davies. H., Randle. V., 2001, The effect of low strain and annealing iterations on the ductility of alpha-brass, Philosophical Magazine A 81, 2553.

Di Leo, C.V., Anand, L., 2013, Hydrogen in metals: A coupled theory for species diffusion and large elastic–plastic deformations, Int. J. Plasticity, 43, 42.

Diard, O., Lecercq, S, Rousselier, G., Cailetaud, G., 2005, Evaluation of finite element based analysis of 3D multicrystalline aggregates plasticity: application to crystal plasticity model identification and the study of stress and strain fields near grain boundaries, Int. J. Plasticity, 21, 691.

Fionova, L.K., Lisovskii, Yu.A., Watanabe, T., 1996, Grain boundary design and control for electrical and magnetic properties of polycrystalline materials, Materials Letters, 28, 141.

Fischer, F.D., Svoboda, J., 2014, Formation of bubbles by hydrogen attack and elastic–plastic deformation of the matrix, Int. J. Plasticity, 63, 110.

Fontana, M.G., Corrosion Engineering, 3rd ed. 1986, McGraw- Hill Book Company, NY.

Francis, P.F and Furrer, D., 2014, 'Lessons Learned from the Development, Application and Advancement of Alloy 718', Proceeding of the 8th International Symposium on Superalloy 718 and Derivatives, TMS (The Minerals, Metals and Materials Society), 28th September- 1st October 2014, Pittsburgh, Pennsylvania, USA, 3.

Fukushma, H., Birnbaum, H.K., 1984, Surface and grain boundary segregations of deuterium in nickel, Acta Metall, 32, 851 .

Haldipur, P., Material characterization of nickel-based super alloys through ultrasonic inspection, PhD Thesis, Iowa State University, USA, (2006).

Haldipur, P., Margetan, F. J., Thompson, R. B., 2004, Estimation of single-crystal elastic constants from ultrasonic measurements on polycrystalline specimens, API Conf. Proc., Wisconsin, USA, 700, 1061.

Harris, T.M., 1989, "Hydrogen Diffusion and Trapping in Electrodeposited Nickel", PhD Thesis, Massachusetts Institute of Technology, USA.

Hicks, P., Alstetter, C., 1992, Hydrogen-enhanced cracking of superalloys, Metall. Trans. A 23, 237.

Jebaraj, J.J.M., Morrison, D.J., Suni, I.I., 2014, Hydrogen diffusion coefficients through Inconel 718 in different metallurgical conditions, Corr. Sci., 80, 517.

Jothi, S., Croft, T.N., Brown, S.G.R., 2014a, Influence of grain boundary misorientation on hydrogen embrittlement in bi-crystal nickel, Int. J Hydrogen energy, 39, 20671.

Jothi, S., Croft, T.N., Brown, S.G.R., de Souza Neto, E.A., 2014b, Finite element microstructural homogenization techniques and intergranular, intergranular microstructural effects on effective diffusion coefficient of heterogeneous polycrystalline composite media, Composite Structures, 108, 555.

Jothi, S., Multiscale modelling and experimentation of hydrogen embrittlement in aerospace materials, PhD Thesis, Swansea University, UK, (2015).

Jothi, S., Croft, T.N., Brown, S.G.R., 2015a, Coupled macroscale-microscale model for hydrogen embrittlement in polycrystalline materials, Int. J. Hydrogen Energy, 40, 2882.

Jothi, S., Croft, T.N., Brown, S.G.R., 2015b, Modelling the influence of microstructural morphology and triple junctions on hydrogen transport in nanopolycrystalline nickel, Composites Part B: Engineering, 75, 104.

Jothi, S., Croft, T.N., Brown, S.G.R., 2015c, Multiscale multiphysics model for hydrogen embrittlement in polycrystalline nickel, J. Alloys and Compounds, In press: DOI:10.1016/j.jallcom.2014.12.073.

Jothi, S., Croft, T.N., Brown, S.G.R., 2015d, "EU FP7 Multi-Scale Modelling Hydrogen Embrittlement - MultiHy", Swansea University deliverable 6.3 report.

Jothi, S., Thuvander, M., 2015e, Atomic analysis of grain boundary segregations in nickel based super alloy using atom probe tomography, In Preparation.

Jothi, S., Winzer, N, Croft, T.N., Brown, S.G.R., 2015f, Meso-microstructural computational simulation of hydrogen permeation test to calculate intergranular, grain boundary and effective diffusivities, J. Alloys and Compounds, In Press: DOI:10.1016/j.jallcom.2014.12.247.

Jothi, S., Croft, T.N., Wright, L., Turnbull, A., Brown, S.G.R, 2015g, Multi-phase modelling of intergranular hydrogen segregation/trapping for hydrogen embrittlement, Int. J. Hydrogen Energy, 40, 15105.

Jothi, S., Sebald, T., Davies, H.M., Reese, E.D., Brown, S.G.R, 2016, Localized microstructural characterization of a dissimilar metal electron beam weld joint from an aerospace component, Materials & Design, 90, 101.

Jothi, S., EU FP7 MultiHy project report (2015h).

Kebir, O.E., Szummer, A., 2002, Comparison of hydrogen embrittlement of stainless steels and nickel-based alloys, Int. J. Hydrogen energy, 27, 793.

Kobayashi, S., Inomata, T., Kobayashi, H., Tsurekawa, S., Watanabe, T., 2008, Effects of grain boundary- and triple junction-character on intergranular fatigue crack nucleation in polycrystalline aluminium, J Mater. Sci., 43, 3792 .

Kobayashi, S., Maruyama, T., Tsurekawa, S., Watanabe, T., 2012, Grain boundary engineering based on fractal analysis for control of segregation induced intergranular brittle fracture in polycrystalline nickel, Acta Mater., 60, 6200.

Koyama, M., Akiyama, E., Tsuzaki, K., Raabe, D., 2013, Hydrogen assisted failure in a twinning-induced plasticity steel studied under in situ hydrogen charging by electron channeling contrast imaging, Acta. Mater., 61, 4607.

Koyama, M., Springer, H., Merzlikin, S. V., Tsuzaki, K., Akiyama, E., Raabe, D., 2014, Hydrogen embrittlement associated with strain localization in a precipitation-hardened Fe-Mn-Al-C light weight austenitic steel, Int. J. Hydrogen energy, 39, 4634.

Krupp, U., Kane, W.M., Liu, X., Dueber, O., Laird, C., McMahon, C.J. Jr., 2003, The effect of grain boundary engineering type processing on oxygen-induced cracking of IN718, Materials Science and Engineering A 349, 213.

Ladna, B., Birnbaum, H.K., 1987, SIMS study of hydrogen at the surface and grain boundaries of nickel bicrystals, Acta Metall., 35, 1775.

Lee, S., Richards, N., 2003, A grain boundary engineering approach to promote special boundaries in Pb-base alloy, Materials Science and Engineering A 354, 106.

Lehockey, E.M., Palumbo, G., 1997, On the creep behaviour of grain boundary engineered nickel, Materials Science and Engineering A 237, 168.

Lehockey, E.M., Limoges, D., Palimbo, G., Sklarchuk, J., Tomantschger, K., Vincze, A., 1999, On improving the corrosion and growth resistance of positive Pb-acid battery grids by grain boundary engineering, Journal of Power Sources, 78, 79.

Leidermark, D., 2011, Crystal plasticity and crack initiation in a single-crystal nickel-base superalloy, PhD Thesis, Linkoping University, Sweden.

Lejcek, P., 2010, Grain Boundary Segregation in Metals, R. Hull, C.,Jagadish, R.M. Osgood Jr., J. Parisi, Z. Wang, H. Warlimont, Springer, Berlin.

Lin, P., Palumbo, G., Erb, U., Aust, K.T., 1995, Influence of grain boundary character distribution on sensitization and intergranular corrosion of alloy 600, Scr. Met. Mater., 33, 1387.

Liu, L., Tanaka, K., Hirose, A., Kobayashi, K.F., 2002, Effects of precipitation phases on the hydrogen embrittlement sensitivity of Inconel 718, Science and Technology of Advanced Materials, 3, 335.

Lynch, S.P., 2003, Failures of engineering components due to environmentally assisted cracking, Practical Failure Analysis, 3, 33.

Mankins, W.L., Lamb, S., 1990, Metals Handbook, nickel and Nickel Alloys, Vol.2, 10th Ed., ASM International, 428.

Martin, M.L., Somerday, B.P., Ritchie, R.O., Sofronis, P, Robertson, I.M., 2012, Hydrogen-induced intergranular failure in nickel revisited, Acta Mater., 60, 2739.

Masayuki, K., Yoshihiro, K., Takayuki, K., 2007, Three-dimensional local stress analysis on grain boundaries in polycrystalline material. Int. J. Solids and Structures, 44, 3267.

Meyers, M., Chawlu, K., 2009, Mechanical Behaviour of Materials, Second Edition, Cambridge University Press.

Palumbo, G., Aust, K.T., 1990, Structure-dependence of intergranular corrosion in high purity nickel, Acta Met. Mater., 38, 2343.

Palumbo, G., Aust, K.T., 1995, Solute effects in grain boundary engineering, Canadian Metallurgical Quarterly, 34, 165.

Palumbo, G., King, P.J., Aust, K.T., Erb, U., Lichtenberger. P.C., 1991, Grain boundary design and control for intergranular stress corrosion resistance, Scr. Met. Mater., 25, 1775 .

Pouillier, E., Gourgues, A.-F., Tanguy, D., Busso, E.P., 2012, A study of intergranular fracture in an aluminium alloy due to hydrogen embrittlement, Int. J. Plasticity, 34, 39.

Preli, F., Furrer, D., 2014, 'Lessons Learned from the Development, Application and Advancement of Alloy 718', Proceeding of the 8th International Symposium on Superalloy 718 and Derivatives, TMS (The Minerals, Metals and Materials Society) September 28-October 1, 2014, Pittsburgh, Pennsylvania, USA, p.3

Priester, L., 2012, Grain Boundaries from Theory to Engineering, Springer.

Pumphrey, P.H., 1976, Grain boundary structure and properties, D.A. Chadwick, G.A. Smiths, eds., Academic Press, London, 139.

Qian, M., Lippold, J., 2003, The effect of annealing twin-generated special grain boundaries on HAZ liquation cracking pf nickel based super alloys, Acta Mater., 51, 3351.

Randle, V., 2004, Twinning-related grain boundary engineering, Acta Mater., 52, 4067.

Randle, V., 1996, The Role of the Coincidence Site Lattice in Grain Boundary Engineering, Maney Publishing.

Randle, V., Davies. H., 2001, Evolution of microstructure and properties in alpha-brass after iterative processing, Metallurgical and Materials Transactions A 33, 1853.

Reese, E.D., von Bestenbostel, W., Sebald, T., Paronis, G.,Vanelli, D., Muller, Y.,*JOM* 66 (2014), 368-1376.

Schlögl, S.M., Van der Giessen, E., 2001, Micromechanics of high temperature hydrogen attack, Int. J. Numer. Meth. Eng., 52, 559.

Seita, M., Hanson, J.P., Gradecak, S., Demkowicz, M.J., 2015, The dual role of coherent twin boundaries in hydrogen embrittlement, Nature Communications, 6, DOI:10.1038/ncomms7164.

Song, J., Curtin, W.A., 2013, Atomic mechanism and prediction of hydrogen embrittlement in iron, Nature Mat., 12, 145.

Thaveeprungsriporn, V., Sinsrok, P., Thong-Aram, D., 2001, Effect of iterative strain annealing on grain boundary network of 304 stainless steel, Scr. Mater., 44, 67.

Watanabe, T., 1984, An approach to grain boundary design for strong and ductile materials, Res. Mechanica, 11, 47.

Watanabe, T., 1993, Grain boundary design and control for high temperature materials, Materials Science and Engineering A 166, 11.

Xu, J, Sun, X.K, Liu, Q.Q., Chen, W.X., 1994, Hydrogen permeation behaviour in IN718 and GH761 Superalloys, Metall. Mater. Trans. A 25, 539.

An investigation of micro-mechanism in hydrogen induced cracking in nickel based superalloy 718.

***S.Jothi[1], S. V. Merzlikin[2], J. Andersson[3,4,5], T.N.Croft[1], S. G. R. Brown[1]**

[1]College of Engineering, Bay Campus, Fabian Way, Swansea SA1 8EN, UK
[2]Max-Planck-InstitutfürEisenforschung GmbH, Max-Planck-Straβe 1, 40237 Düsseldorf, Germany
[3]GKN Aerospace Engine Systems, Trollhättan, SE-46181, Sweden
[4]Department of Engineering Science, University West, Trollhättan, SE-46186, Sweden
[5]Department of Materials and Manufacturing Technology, Chalmers University of Technology, Gothenburg, SE-412 96, Sweden

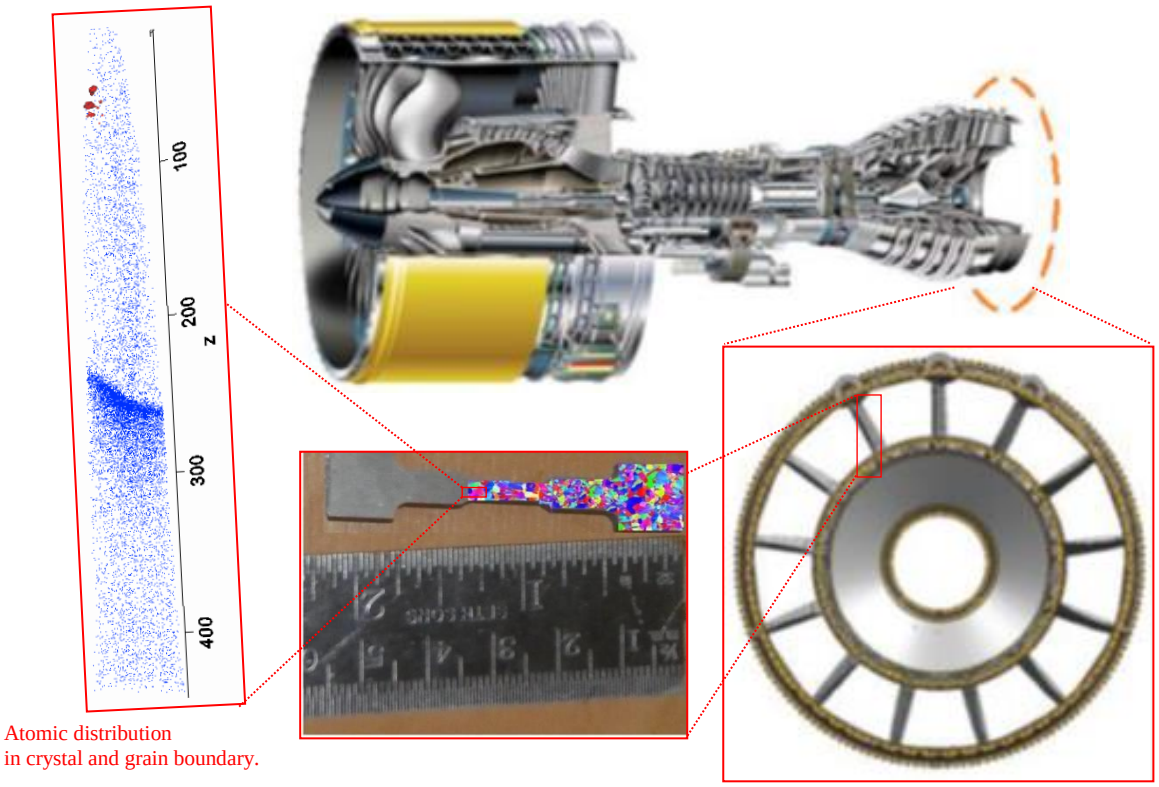

Figure 1. An example of a commercial aero engine with load carrying alloy 718 structures in the rear part of the GP7000 engine and the sample specimen used for this investigation.

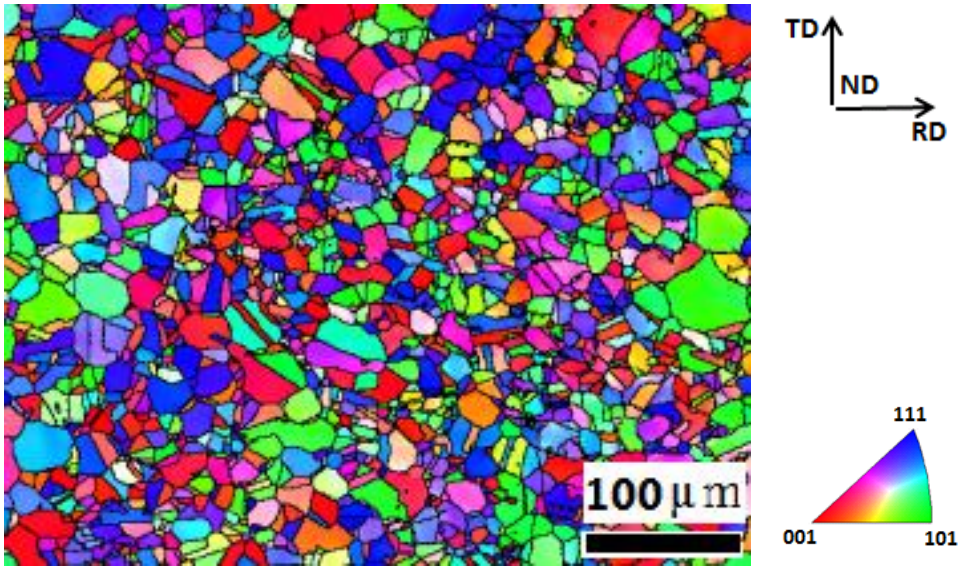

(a)

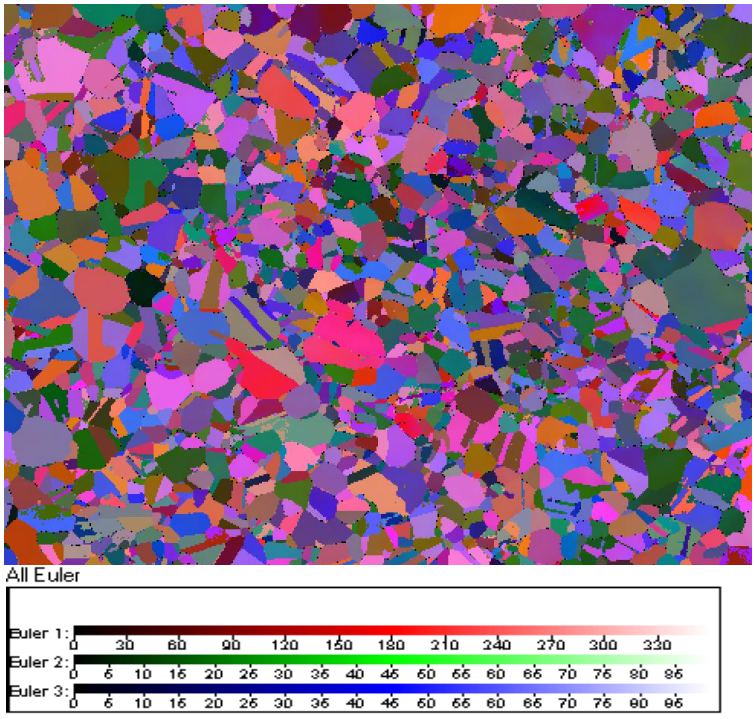

(b)

Figure 2. Microstructure of the undeformed solution heat treated Alloy 718. (Readers are referred to the web version on this article for the interpretation of the reference to colour in the figure legend.) (a) IPF figure of the undeformed material microstructure and grain morphology and (b) Crystal orientations in Euler angles.

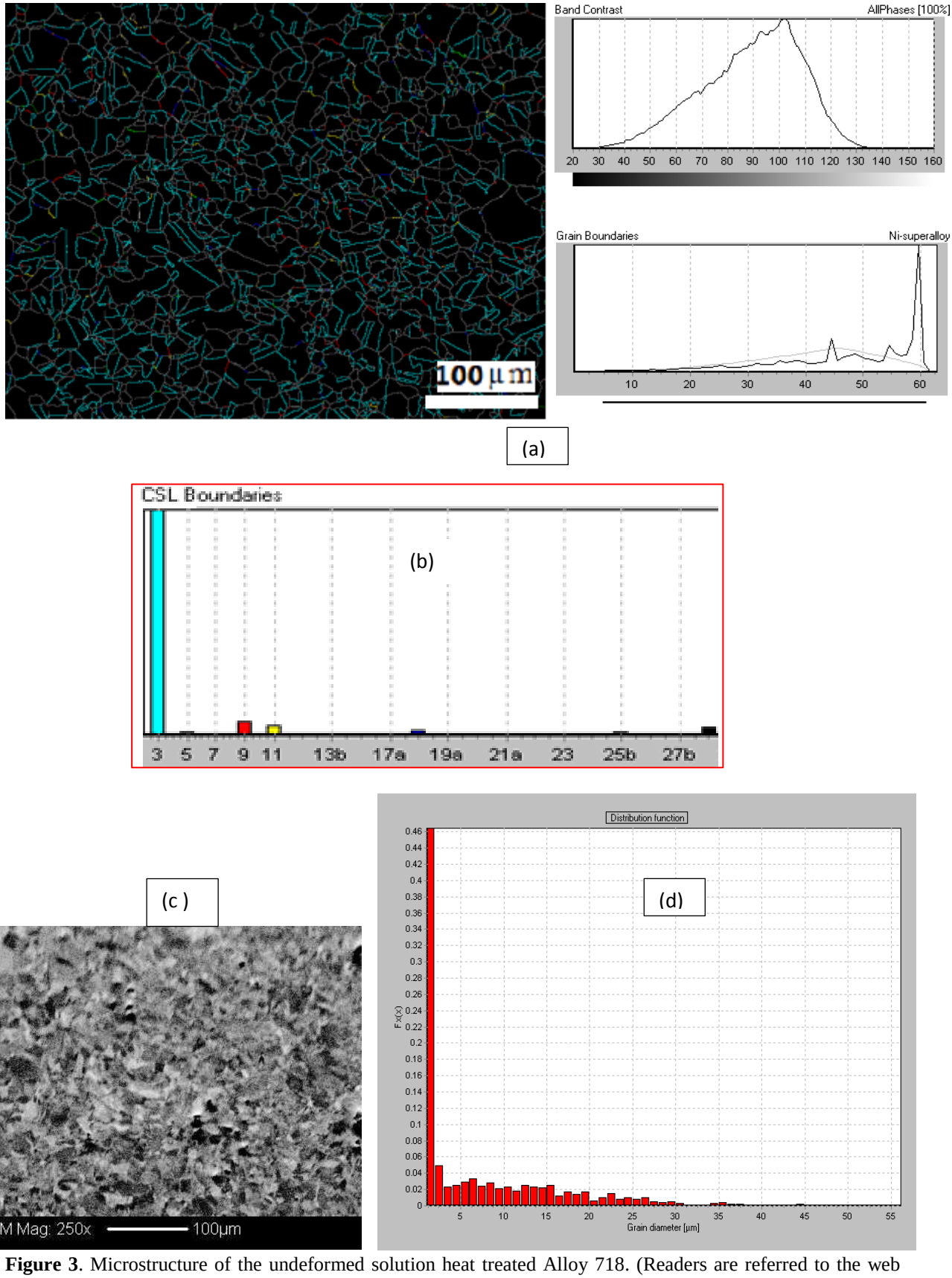

Figure 3. Microstructure of the undeformed solution heat treated Alloy 718. (Readers are referred to the web version on this article for the interpretation of the reference to colour in the figure legend.) (a) Special Coincidence site lattice (CSL) grain boundaries (with grain boundary misorientations Σ less than 29°). (b) CSL statistics (c.f. Table 1 for corresponding percentages), (c) SEM back scattering electron (BSE) image of the undeformed microstructure and (d) grain diameter distribution of the undeformed microstructure.

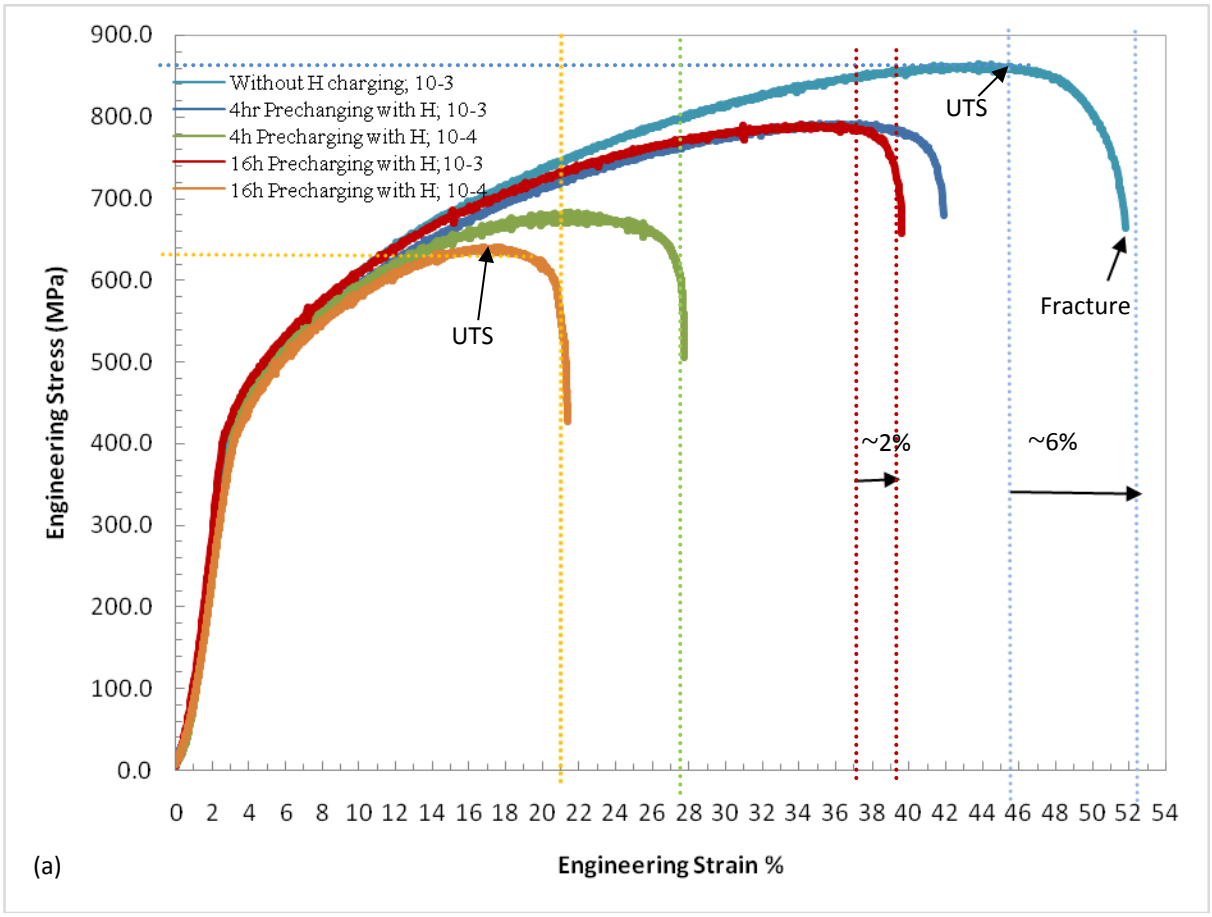

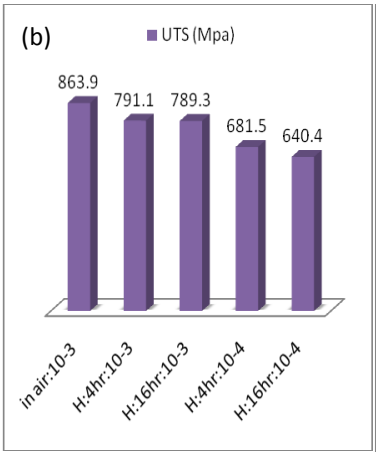

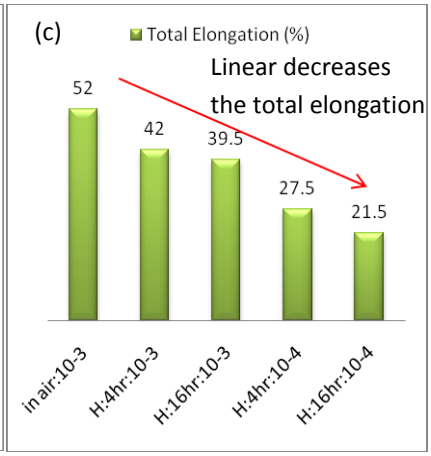

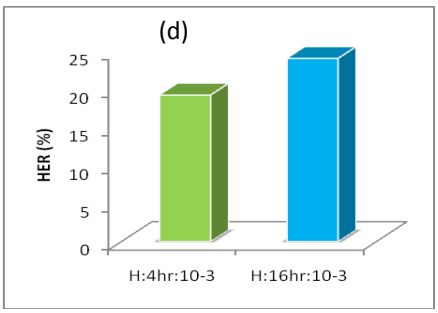

Figure 4. (a) Results of the slow strain rate tests of Alloy 718 uncharged and tested in air and with 4 or 16 hours pre-charging and in-situ hydrogen charging during testing for strain rates of 10^{-3} s^{-1} and $10^{-4}s^{-1}$. (b) Variation of ultimate tensile strength for different test conditions. (c) Variation of total percentage elongation to fracture for different testing conditions. (d) The effect of hydrogen charging time on the hydrogen embrittlement ratio.

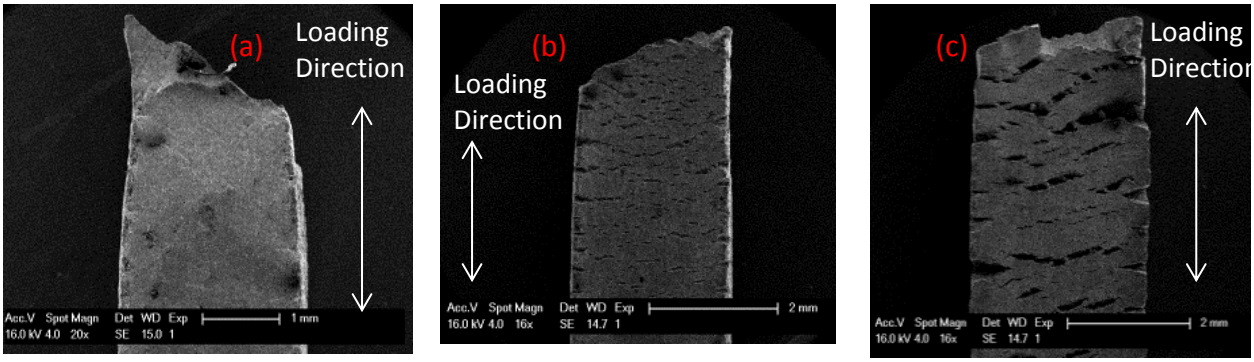

Figure 5.Scanning electron microscope (SEM) secondary electron (SE) images of fracture surface morphologies along the loading direction. (a) Uncharged sample tested in air (No secondary surface cracks were observed). (b) and (c) samples tested in the 16 hours pre-charged condition with in-situ hydrogen charging for tests at strain rates of 10^{-3} $s^{-1}$and 10^{-4} s^{-1} respectively (Numerous secondary surface cracks were observed).

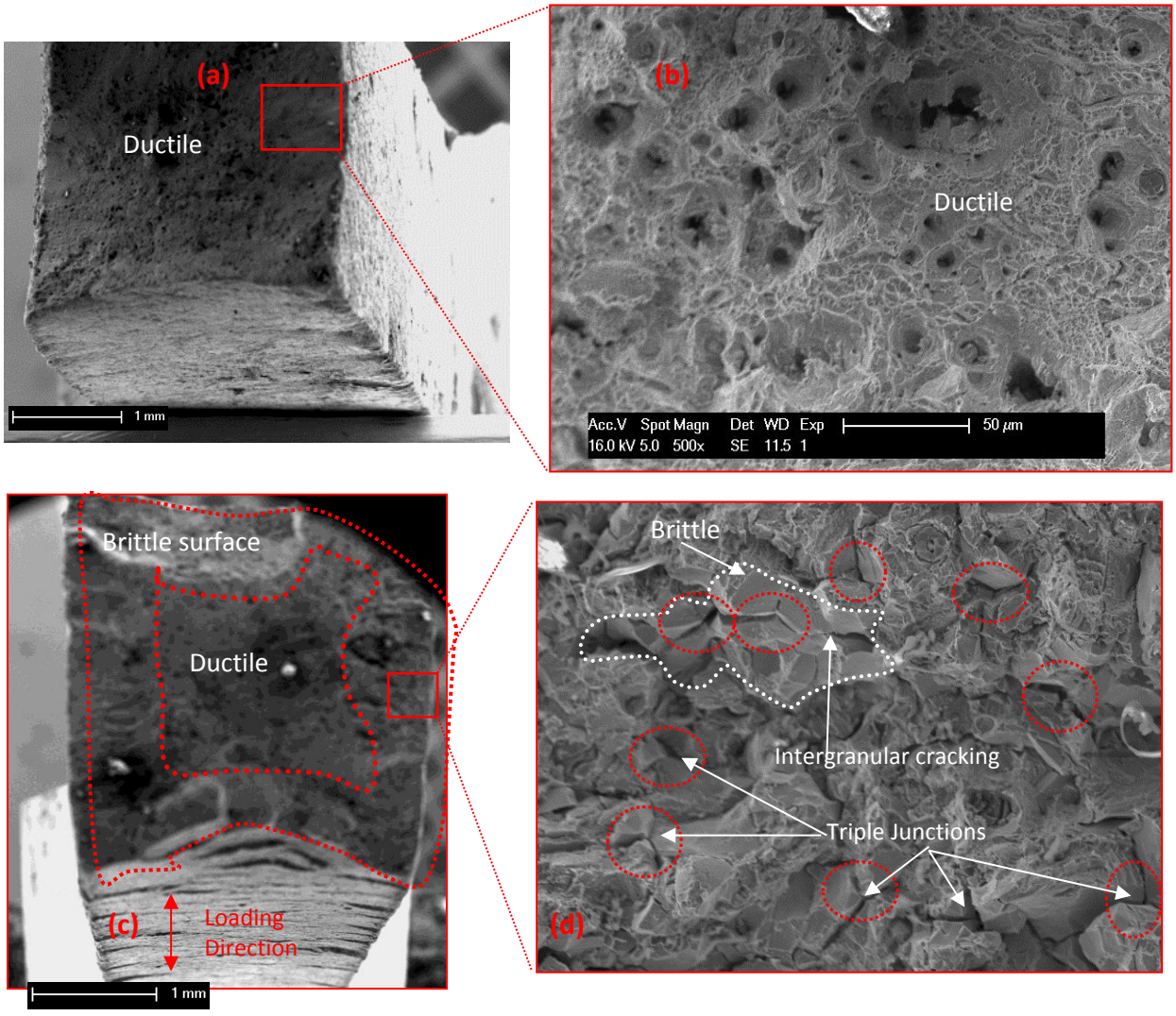

Figure 6. (a) and (b) are secondary electron images of the fracture specimen normal to the loading direction of the uncharged sample tested in air. (b) A typical ductile fracture mode. (c) and (d) show a fracture specimen tested in the hydrogen charging condition normal to the loading direction. (d) A typical brittle fracture mode in the hydrogen charged sample displaying intergranular cracking and indicating triple junctions are more susceptible to hydrogen induced cracking and appear to be crack initiation points (dotted red circles).

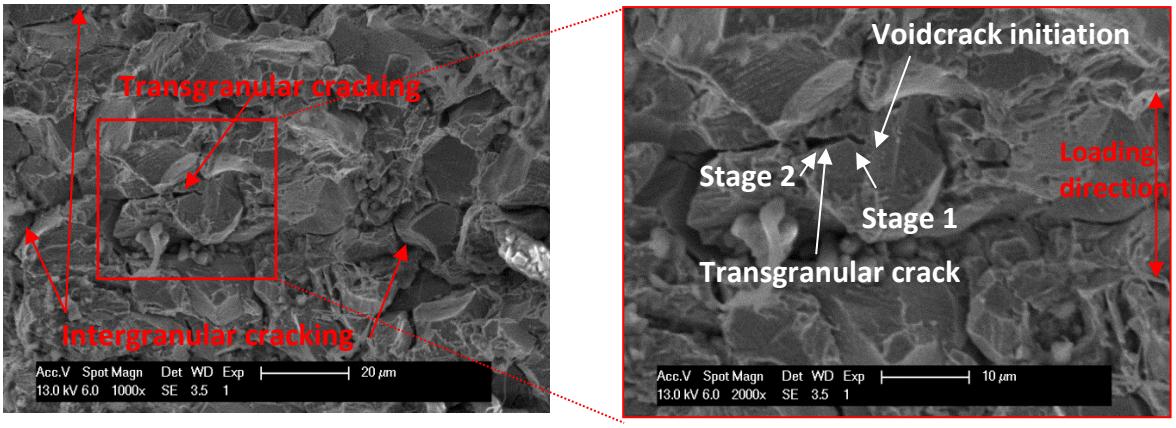

(a) (b)

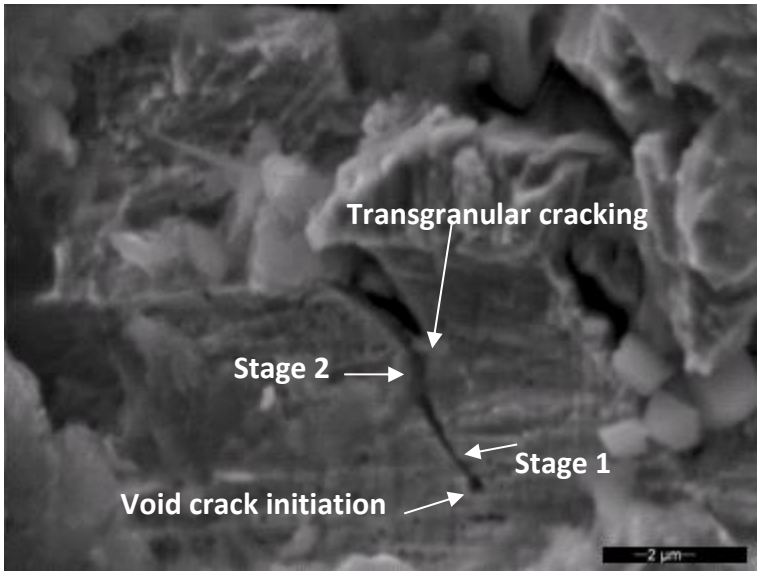

(c)

Figure 7. SEM fractography images for hydrogen charged Alloy 718 material. (a) Intergranular and Transgranular cracking. (b) and (c) show magnified views of transgranular cracking.

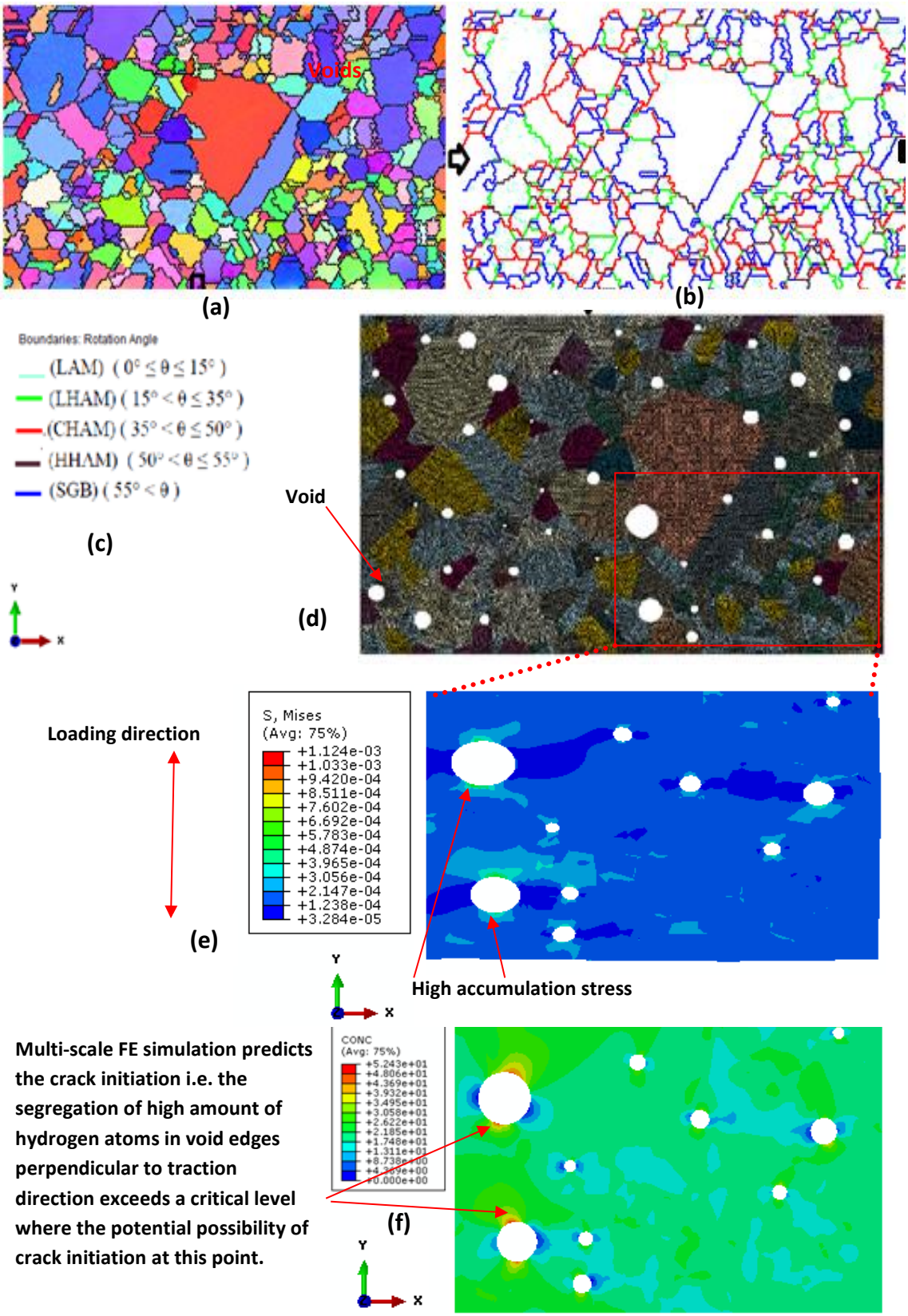

Figure8. (a) Microstructural image developed from EBSD machine data source, (b) Grain boundary characteristic distribution developed from EBSD machine data source, (c) Real microstructural representative finite element model with mesh developed by incorporating the EBSD machine data source, random void on the grain boundaries in ABAQUS using MATLAB, PYTHON and FE coding. (d) Multiscale FE stress analysis results show the stress distribution (Stress values in N/μm^2). (e) Multiscale FE stress & dislocation assisted

hydrogen diffusion analysis result shows the hydrogen distribution at the micro-level which predicts the potential crack initiation sites near void edges perpendicular to the traction direction.

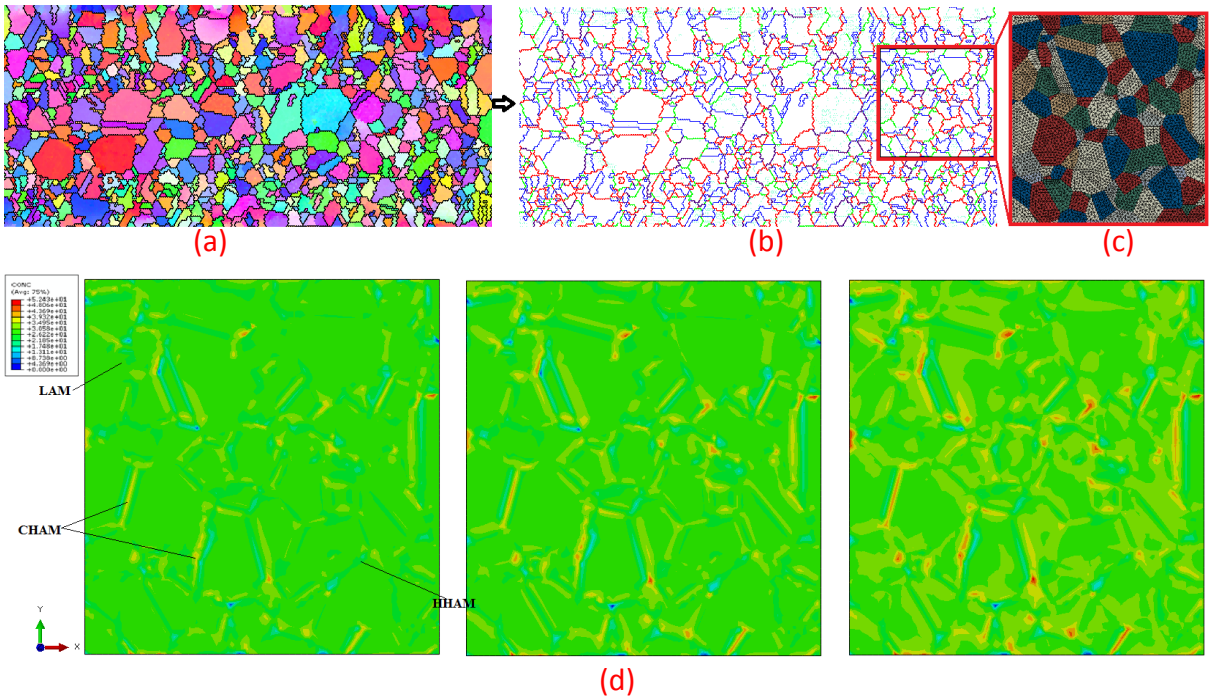

Figure 9 (a) Shows the EBSD result of IN718 microstructure, (b) shows the grain boundary misorientation types (i.e please refer figure 5 (d) for grain boundary misorientation types colour code), (c) shows the microscale real microstructural representative volume element FE model developed in ABAQUS and (d) Chemo-mechanical-dislocation real microstructural RVE model based computational multiscale simulation results shows hydrogen segregation in various types of grain boundary misorientation on the IN718 microstructure after three different increasing times (i.e from left to right).

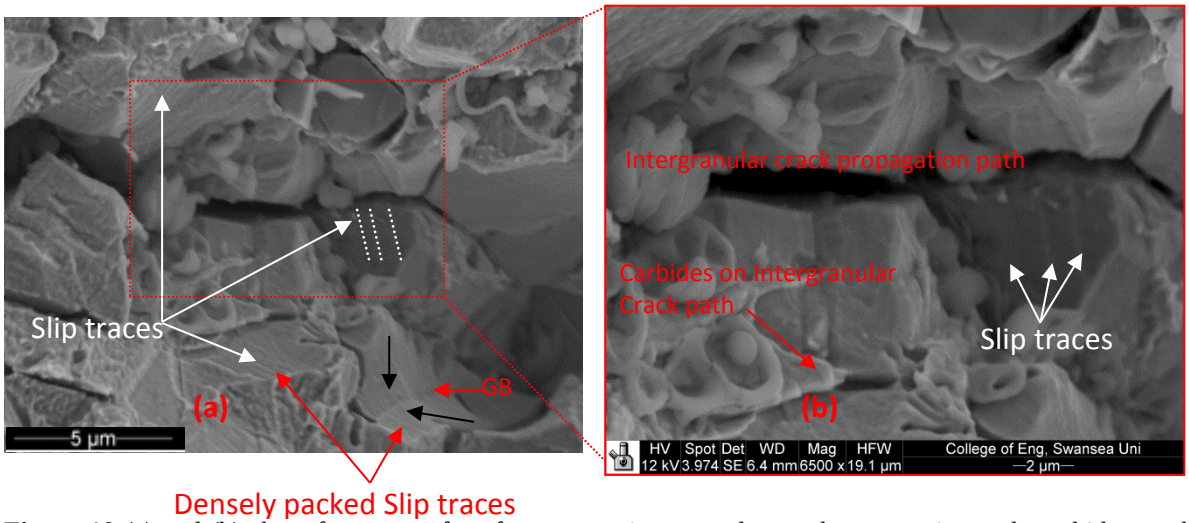

Figure 10 (a) and (b) show fracture surface features: an intergranular crack propagation path, carbides on the intergranular crack path and slip traces on surfaces.

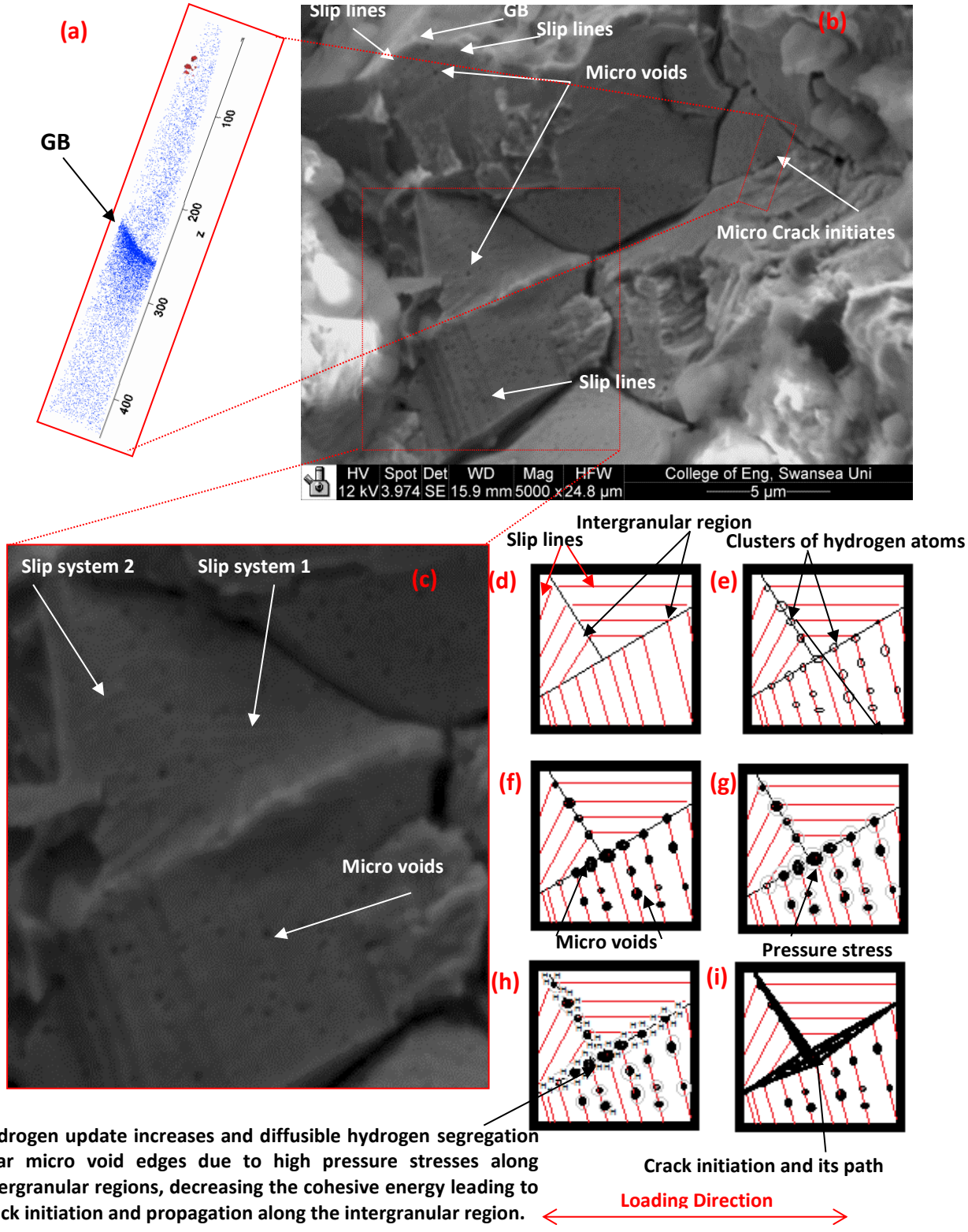

Figure 11. (a) Segregation of carbon atoms to the grain boundary in Alloy 718 using atom probe tomography. (b) Micro crack initiation along a grain boundary. (c) Slip traces and micro voids along grain boundaries. (d) Relationship between slip traces (red lines) and intergranular region (black lines). (e) Segregation of hydrogen clusters (black open circles) on slip lines. (f) Formation of micro voids (black filled circles) on the hydrogen

clusters forming at slip band sites. (g) Developing high pressure stresses around void edges (grey circles around black filled circles). (h) Trapping of hydrogen (H-symbols) around micro-voids due to tensile stresses and the high gradient of pressure perpendicular to the loading direction. (i) Crack initiation at triple junctions and/or near larger micro-void edge regions perpendicular to the traction direction propagating by coalescence of micro-voids along intergranular regions due to the increase in pressure in micro voids.

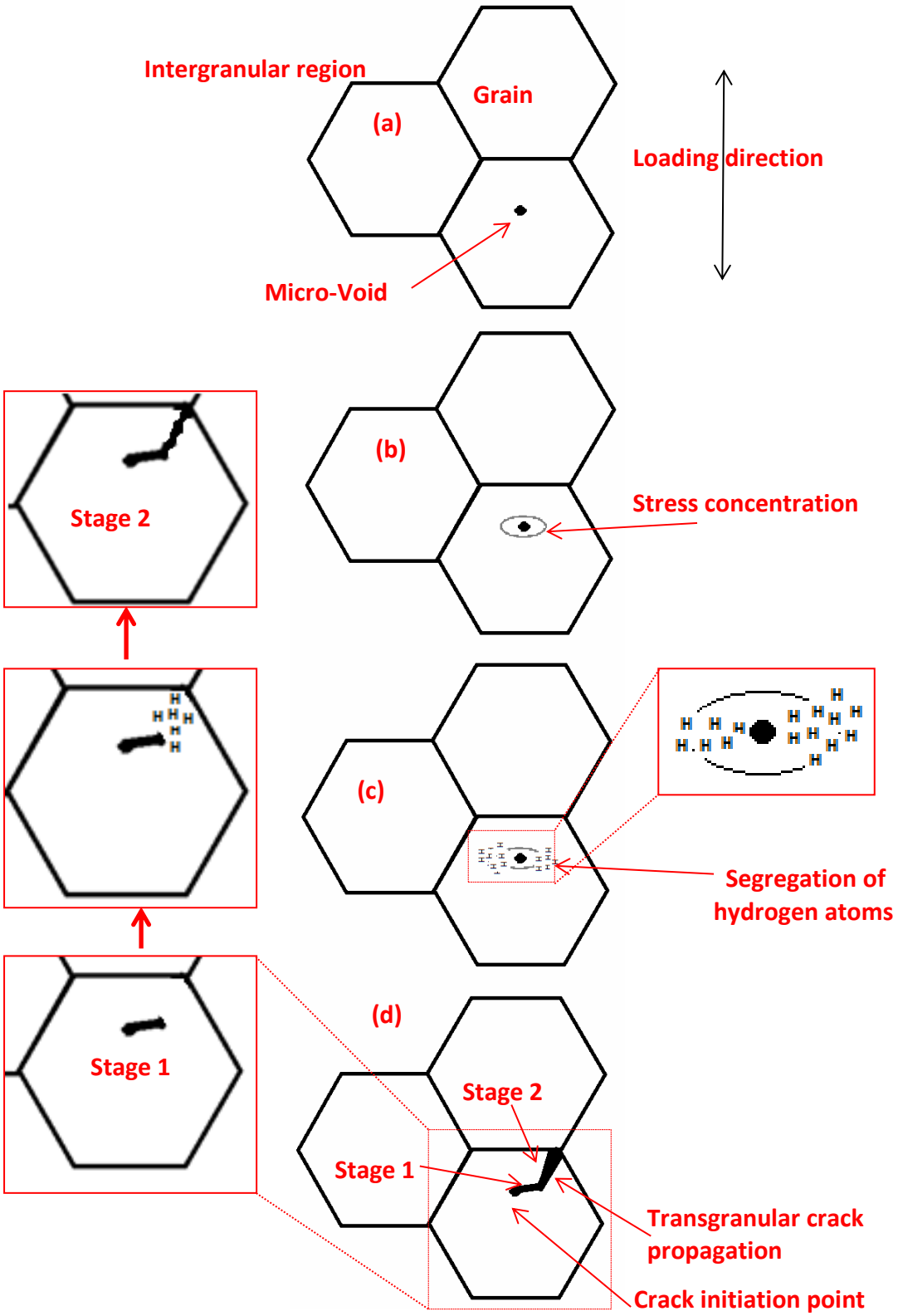

Figure 12.Schematic illustration of possible pore/void dependent hydrogen induced transgranular cracking mechanism in Alloy 718. (a) Polycrystalline material with micro-pores before transgranular cracking. (b) Stress concentration greater perpendicular to the traction direction as opposed to parallel. (c) The tensile stress concentrations around deformed pores/voids increases the mobility of hydrogen atoms which become trapped in these tensile stress concentration sites. The amount of trapped hydrogen will be greater in near-void regions perpendicular to loading direction. (d) Illustrates the proposed model of a transgranular crack initiation site and two stage propagation path.

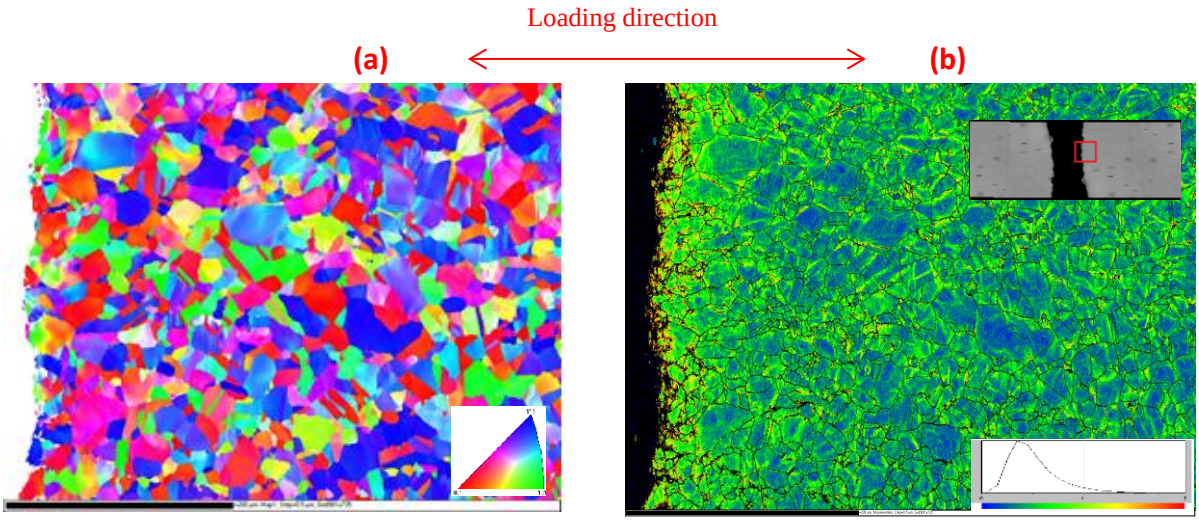

Figure13. EBSD results for the uncharged SSRT fractured specimen. (a) Crystallographic orientation and IPF information in the loading direction. (b) Local misorientation map and colour contour (red colour regions have the largest misorientations and blue colour regions the smallest).

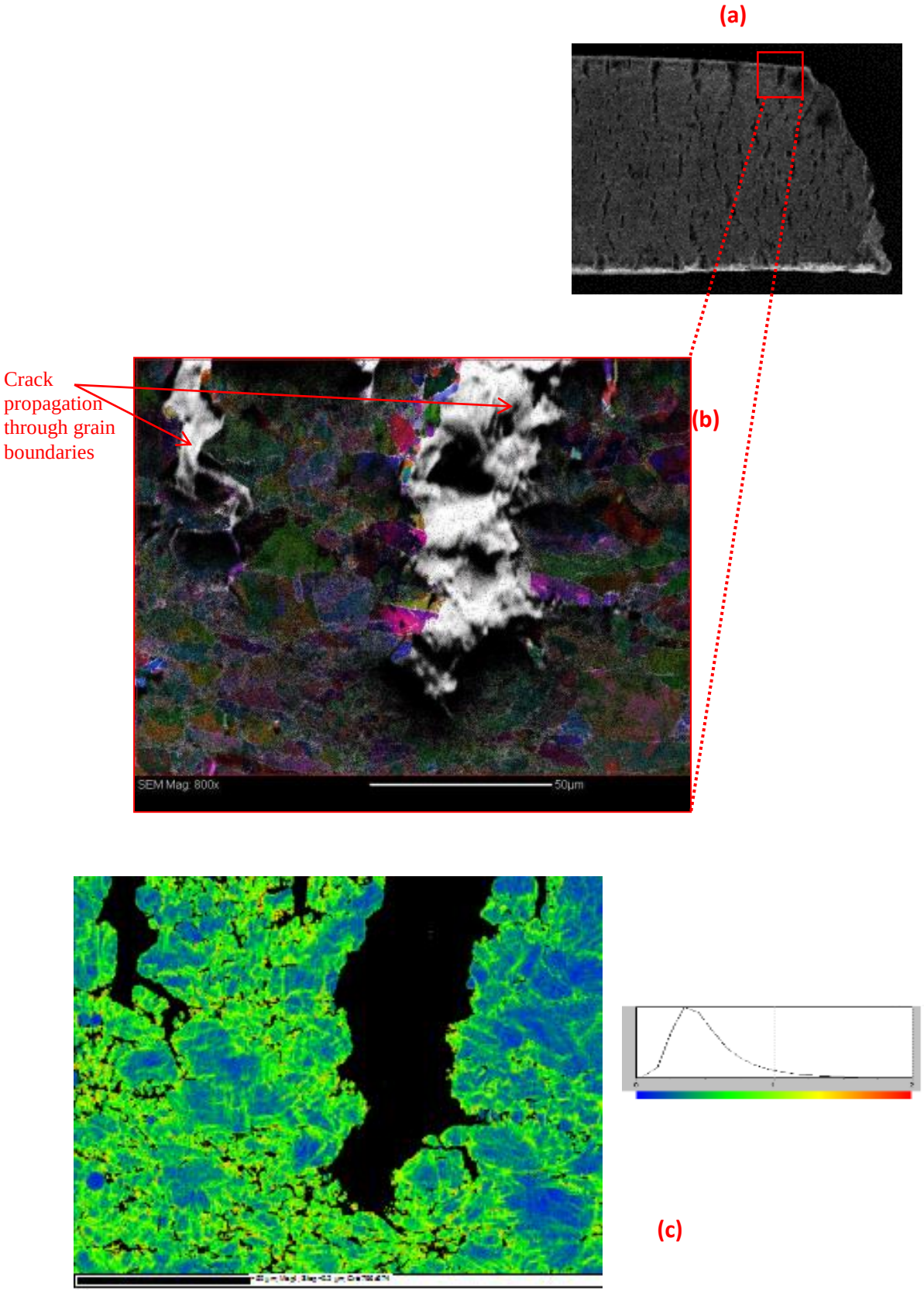

Figure 14. (a) Hydrogen charged SSRT tested fractured specimen. (b) EBSD map overlaid on SEM micrograph and (c) Local misorientation map and colour contour.

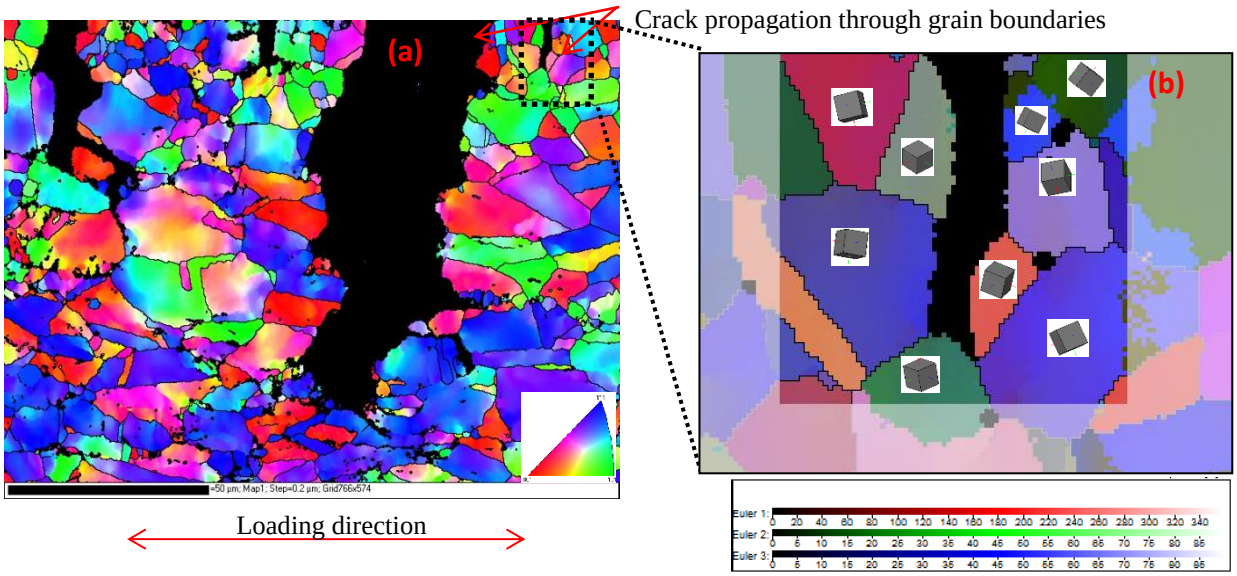

Figure15. (a) Crystallographic orientation and IPF information in the loading direction and (b) Closer view near crack region and Euler angles.

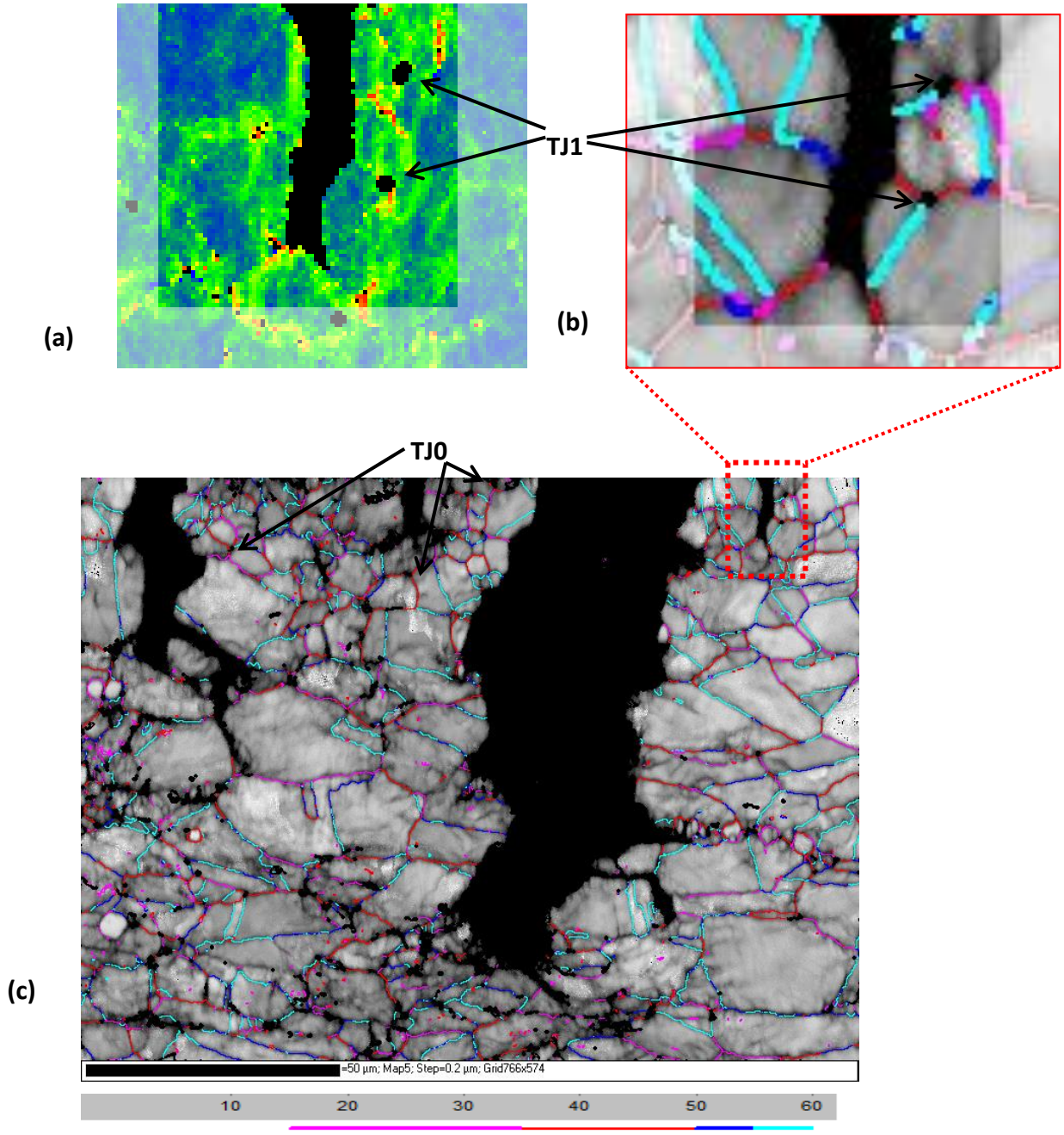

Figure16. (a) Close view of local misorientation on hydrogen induced crack path, (b) Close up view of grain boundary characteristic distribution at a hydrogen induced crack path (c) Grain boundary characteristic distribution at a hydrogen induced crack path.

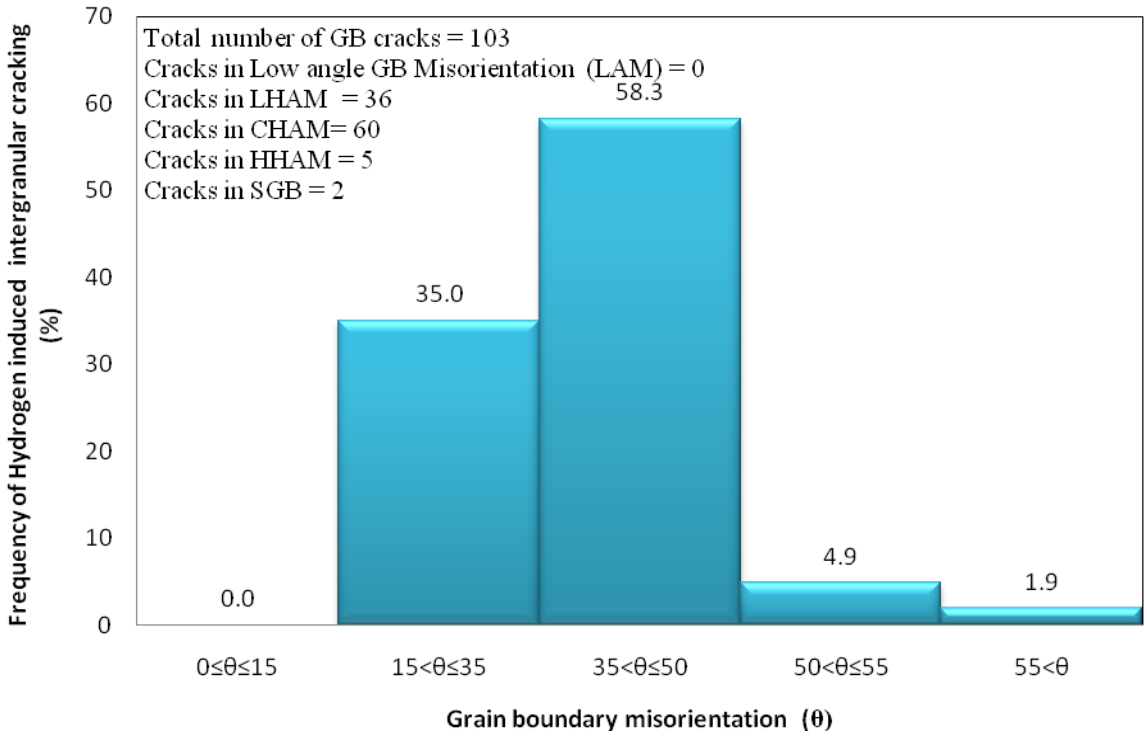

Figure17. Relationship between grain boundary characteristics and observed hydrogen induced intergranular cracking.

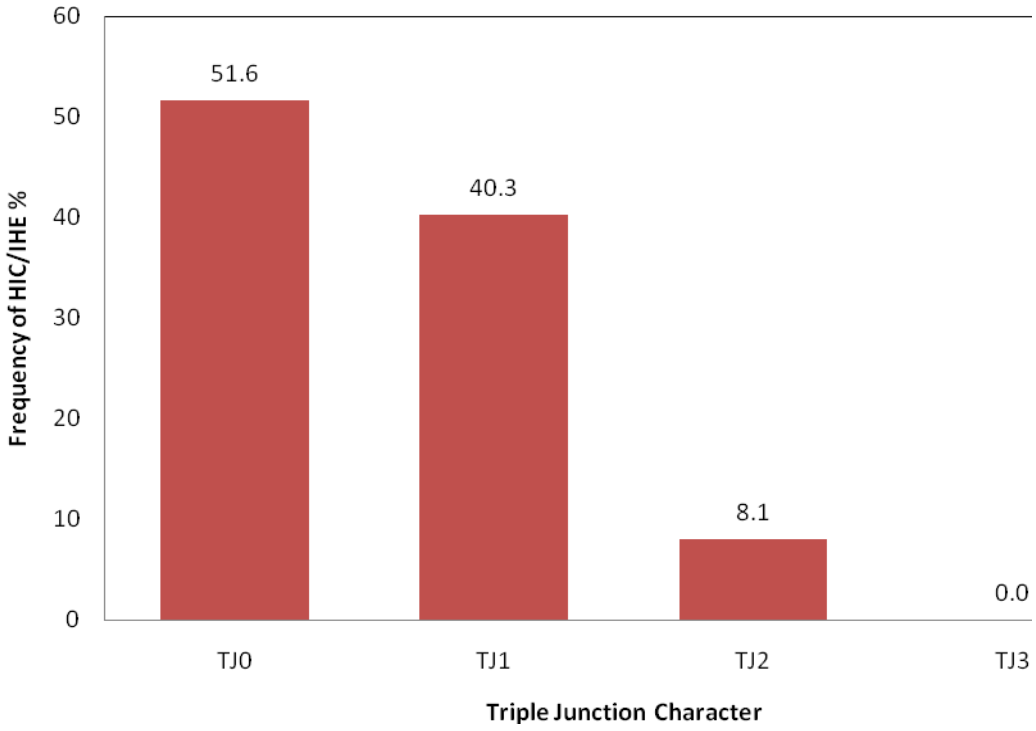

Figure18. Relationship between triple junction characteristics and observed hydrogen induced intergranular cracking.